






# Unraveling the Mystery of the Low CO-to-H<sub>2</sub> Conversion Factor in Starburst Galaxies: RADEX Modeling of the Antennae

HAO HE <sup>1</sup>, CHRISTINE WILSON <sup>1</sup>, JIAYI SUN <sup>2,1</sup>, YU-HSUAN TENG <sup>3</sup> AND ERIK ROSOLOWSKY <sup>4</sup>

<sup>1</sup>*McMaster University, 1280 Main St. W., Hamilton, ON., L8S 4L8, Canada*

<sup>2</sup>*Department of Astrophysical Sciences, Princeton University, 4 Ivy Lane, Princeton, NJ 08544, USA*

<sup>3</sup>*Center for Astrophysics and Space Sciences, Department of Physics, University of California San Diego, 9500 Gilman Drive, La Jolla, CA 92093, USA*

<sup>4</sup>*Department of Physics, University of Alberta, Edmonton, AB T6G 2E1, Canada*

Submitted to ApJ

## ABSTRACT

CO emission has been widely used as a tracer of molecular gas mass. However, it has been a long-standing issue to accurately constrain the CO-to-H<sub>2</sub> conversion factor ( $\alpha_{\text{CO}}$ ) that converts CO luminosity to molecular gas mass, especially in starburst galaxy mergers. We present the first resolved  $\alpha_{\text{CO}}$  modeling results with multiple ALMA CO and <sup>13</sup>CO transition observations at both giant molecular cloud (GMC) scale down to 150 pc and kpc scale for one of the closest starburst mergers, the Antennae. By combining our CO modeling results and measurements of 350 GHz dust continuum, we find that most GMCs in the Antennae have  $\alpha_{\text{CO}}$  values  $\sim 4$  times smaller than the commonly adopted Milky Way value of 4.3. We find  $\alpha_{\text{CO}}$  at GMC scales shows a strong dependence on CO intensity, <sup>13</sup>CO/CO ratio and GMC velocity dispersion, which is consistent with various theoretical and simulation predictions. Specifically, we suggest that <sup>13</sup>CO/CO line ratio and the velocity dispersion can be used to calibrate  $\alpha_{\text{CO}}$  in starburst regions. By applying our modeled  $\alpha_{\text{CO}}$  in GMC analyses, we find that GMCs in the Antennae are less gravitationally bound than in normal spiral galaxies, which is more consistent with what is predicted by merger simulations. At kpc scale, we find that our modeled  $\alpha_{\text{CO}}$  values are smaller than the modeled  $\alpha_{\text{CO}}$  at GMC scale by 40%, which can be due to inclusion of diffuse gas component with lower  $\alpha_{\text{CO}}$ . We also find a similar correlation of  $\alpha_{\text{CO}}$  and CO intensity at kpc scale to that at GMC scale.

*Keywords:* Molecular gas (1073), Molecular clouds (1072), CO line emission (262), Starburst galaxies (1570), Galaxy mergers (608)

## 1. INTRODUCTION

The cold and dense molecular gas in the interstellar medium (ISM) is the direct fuel for current and future star formation. Measuring the amount and properties of the molecular gas is crucial for understanding star formation, the ISM, and their relations with galaxy evolution. Although H<sub>2</sub> is the dominant component of molecular gas, it is not normally observable due to the high excitation temperature ( $T_{\text{ex}}$ ) of its lines. Instead, the <sup>12</sup>C<sup>16</sup>O  $J=1-0$  line (hereafter CO  $J=1-0$ ) is the most commonly used tracer for measuring the molecular gas mass via the CO-to-H<sub>2</sub> conversion factor  $\alpha_{\text{CO}}$ . This  $\alpha_{\text{CO}}$  is commonly defined for the  $J = 1-0$  line as the ratio of total molecular gas to ( $M_{\text{mol}}$  in  $M_{\odot}$ ) to the CO  $J=1-0$

luminosity ( $L_{\text{CO}(1-0)}$  in  $\text{K km s}^{-1} \text{pc}^2$ ), or equivalently, the ratio of molecular gas surface density ( $\Sigma_{\text{mol}}$  in  $M_{\odot} \text{pc}^{-2}$ ) to the CO  $J=1-0$  intensity ( $I_{\text{CO}(1-0)}$  in  $\text{K km s}^{-1}$ ):

$$\alpha_{\text{CO}} = \frac{M_{\text{mol}}}{L_{\text{CO}(1-0)}} = \frac{\Sigma_{\text{mol}}}{I_{\text{CO}(1-0)}} \left[ \frac{M_{\odot}}{\text{K km s}^{-1}} \right] \quad (1)$$

Given that CO is so straightforwardly observable, a concrete prescription for  $\alpha_{\text{CO}}$  as a function of local ISM properties has been a longstanding goal.

$\alpha_{\text{CO}}$  is first calibrated for individual giant molecular clouds (GMCs) in our Milky Way based on virial methods (e.g. Solomon et al. 1987; Scoville et al. 1987; Scoville & Good 1989; Maloney 1990; Young & Scoville 1991), optically thin tracers such as dust continuum (Boulanger

et al. 1996; Dame et al. 2001; Planck Collaboration et al. 2011), CO isotopologue lines (Goldsmith et al. 2008) and gamma-ray observations (e.g. Strong & Mattox 1996; Grenier et al. 2005; Abdo et al. 2010). These studies have found a relatively constant  $\alpha_{\text{CO}}$  around  $4.3 M_{\odot} (\text{K km s}^{-1} \text{ pc}^2)^{-1}$  (Bolatto et al. 2013, and references therein) with scatter of 0.3 dex. However, systematic variations of  $\alpha_{\text{CO}}$  have been found in our Milky Way, specifically for GMCs in the central molecular zone (CMZs) where  $\alpha_{\text{CO}}$  can be 3 – 10 times lower than the average value (Bolatto et al. 2013, and references therein). Furthermore, extra-galactic observations have found systematic variations of  $\alpha_{\text{CO}}$  up to one or two orders of magnitude across different galactic environments (e.g. Bolatto et al. 2008; Donovan Meyer et al. 2012; Rebolledo et al. 2012; Sandstrom et al. 2013a). This issue is further complicated by the fact that different calibration methods can lead to vastly discrepant estimates of  $\alpha_{\text{CO}}$  values (e.g. SMC Bolatto et al. 2003; Leroy et al. 2011). Therefore, assuming a constant  $\alpha_{\text{CO}}$  can introduce systematic bias in calculating molecular gas mass and surface density and related quantities, such as molecular gas depletion time, the cloud free-fall time, the virial parameter and the turbulent pressure (Sun et al. 2022, 2023).

Theoretical models and simulations suggest that  $\alpha_{\text{CO}}$  can be dependent on both small-scale GMC properties, such as temperature, volume and surface density (Gong et al. 2020; Hu et al. 2022, and references therein), and kpc-scale environmental properties, such as metallicity, galactic disk surface density (e.g. Wolfire et al. 2010; Narayanan et al. 2012; Kazandjian et al. 2015; Renaud et al. 2019a; Hu et al. 2022). Recently, a lot of progress has been made in calibrating metallicity dependence of  $\alpha_{\text{CO}}$  (e.g. Schrubba et al. 2012; Amorín et al. 2016; Accurso et al. 2017), which has been applied to several recent works (e.g. Sun et al. 2020a,b; Pessa et al. 2021; Sun et al. 2023). However, we still lack a general  $\alpha_{\text{CO}}$  prescription that incorporates all the related physical quantities at different scales.

In particular,  $\alpha_{\text{CO}}$  in starburst systems, such as ultra/luminous infrared galaxies (U/LIRGs), is poorly constrained. Early studies (e.g. Downes et al. 1993; Bryant & Scoville 1996, 1999; Solomon et al. 1997; Downes & Solomon 1998) find that  $\alpha_{\text{CO}}$  in U/LIRGs should be  $\sim 4$  times lower than the Milky Way value to give a reasonable molecular gas mass values within the dynamical mass range. Studies on a large sample of U/LIRGs using multi-CO line large velocity gradient (LVG) radiative transfer modeling (e.g. Solomon & Vanden Bout 2005; Downes & Solomon 1998; Papadopoulos et al. 2012) find consistent average  $\alpha_{\text{CO}}$  values around 1.1

$M_{\odot} (\text{K km s}^{-1} \text{ pc}^2)^{-1}$  (Downes & Solomon 1998, with helium contribution). Therefore, a discrete bimodal  $\alpha_{\text{CO}}$  prescription or a modified version accounting for the deviation from the star-forming main sequence (e.g. Magnelli et al. 2012; Sargent et al. 2014) is generally applied in observed normal spiral and starburst galaxies. However, there is likely a large galaxy-to-galaxy  $\alpha_{\text{CO}}$  variation for different U/LIRGs (Papadopoulos et al. 2012; Sliwa et al. 2017a; Carleton et al. 2017), which is not captured by those  $\alpha_{\text{CO}}$  prescriptions. This problem is further complicated by recent works using optically thin tracers (e.g. Dunne et al. 2022), which suggest a Milky-Way like  $\alpha_{\text{CO}}$  value for these U/LIRGs.

Besides galaxy-to-galaxy variation, theoretical works (Narayanan et al. 2012; Bolatto et al. 2013) also suggest that  $\alpha_{\text{CO}}$  could vary within galaxies depending on the local environment. Therefore, it is crucial to understand the physical driver of the low  $\alpha_{\text{CO}}$  in these starburst systems. Narayanan et al. (2011) suggest that the low  $\alpha_{\text{CO}}$  is caused by the increase in GMC temperature (partly through thermal coupling with dust heated by UV radiation; Magnelli et al. 2012; Olsen et al. 2016) and/or velocity dispersion (out of self-gravity; Papadopoulos et al. 2012), which makes CO emission over-luminous. Recent galaxy merger observations (e.g. Papadopoulos et al. 2012) and simulations (e.g. Bournaud et al. 2015) seem to favor the increase in velocity dispersion to play the major role. However, Renaud et al. (2019b) show in their simulation that  $\alpha_{\text{CO}}$  is not a sole function of velocity dispersion and is also dependent on different merging stages. To disentangle these factors, it is crucial to constrain the GMC physical properties and dynamical states in observed starburst mergers among different stages.

In order to diagnose GMCs physical states and reasons for  $\alpha_{\text{CO}}$  variation, it is necessary to observe multiple CO and other molecular lines (specifically optically thin lines) at GMC resolution ( $\sim 100$  pc) to perform comprehensive LVG modeling. This approach has recently been implemented across several nearby galaxy centers (e.g. Teng et al. 2022; Teng et al. 2023). However, due to the limited sensitivity and resolution of current instruments, most LVG studies on individual starburst mergers (e.g. Papadopoulos et al. 2012; Sliwa et al. 2012, 2013, 2014; He et al. 2020) can only probe a limited number of gas-rich regions at kpc resolution, making it hard to extract any  $\alpha_{\text{CO}}$  dependence on GMC properties and local environments. As one of the closest starburst mergers, NGC 4038/9 (the Antennae) is an ideal target for this study. At a distance of 22 Mpc (Schweizer et al. 2008), ALMA can readily resolve molecular gas at GMC scales. The total SFR of the Antennae is between  $11 M_{\odot} \text{ yr}^{-1}$  (es-

timated from UV and 24  $\mu\text{m}$  probing  $\sim 1$  to 400 Myr (Bemis & Wilson 2019) and  $20 M_{\odot}\text{yr}^{-1}$  (estimated from extinction corrected  $\text{H}\alpha$  probing  $\sim 1$  to 10 Myr Chandar et al. 2017). Although the Antennae is technically not a LIRG based on its total infrared luminosity, the higher SFR value traced by  $\text{H}\alpha$  is comparable to those of LIRGs, which suggests a starburst event that was just triggered recently several tens of Myr ago. As a typical major merger between two gas-rich galaxies, the Antennae has been well-studied in both simulations and observations. Most simulations (e.g. Karl et al. 2010; Privon et al. 2013; Renaud et al. 2019a) suggest that the Antennae has just passed its second pericentric passage  $\sim 40$  Myr ago. Its central region hosts the two progenitor nuclei, still separated by about 7 kpc (Zhang et al. 2001). As a starburst merger, it also hosts a large number ( $\sim 10^4$ ) of young massive star clusters exceeding  $10^4 M_{\odot}$ , with maximal mass reaching  $10^6 M_{\odot}$  (Whitmore et al. 2014; Mok et al. 2020; He et al. 2022). The extreme number of YMCs will provide much stronger stellar feedback (Keller et al. 2014) that will disperse molecular gas and significantly reduce the  $\alpha_{\text{CO}}$  values (Renaud et al. 2019a).

In this paper, we perform LVG modeling on high-resolution ( $\sim 150$  pc) CO and  $^{13}\text{CO}$  molecular lines from ALMA observations of the Antennae to constrain the physical properties of the molecular gas and  $\alpha_{\text{CO}}$  at both GMC and kpc scales. In Section 2, we describe the observations and how we processed the data. In Section 3, we describe the RADEX modeling method that we used to derive gas physical quantities (e.g. temperature, volume density and CO column density) and  $\alpha_{\text{CO}}$ . In Section 4, we present our modeled gas physical properties (e.g. kinetic temperature, volume density and CO column density) and their connection with different line ratios. In Section 5, we present our modeled  $\alpha_{\text{CO}}$  at GMC scale and compare its dependence on various GMC observational and physical quantities with theoretical, simulation and observational predictions. We also apply our modeled  $\alpha_{\text{CO}}$  in calculation of GMC surface density and virial equilibrium states. In Section 6, we present modeled  $\alpha_{\text{CO}}$  at kpc scales and its comparison with  $\alpha_{\text{CO}}$  at GMC scales. We also explore  $\alpha_{\text{CO}}$  dependence on kpc-scale gas properties (e.g. gas surface density, velocity dispersion and metallicity). The conclusions are summarized in Section 7.

## 2. OBSERVATIONS AND DATA PROCESSING

### 2.1. ALMA Spectral Lines

We use multiple CO lines (CO  $J=1-0$ ,  $2-1$ ,  $3-2$  and  $^{13}\text{CO}$   $J=1-0$ ,  $2-1$ ) from the Atacama Large Millimeter/Submillimeter Array (ALMA) to determine the

physical properties of the gas in the Antennae at 150 pc scale. We obtained ALMA Band 3, 6 and 7 observations from cycle 5 project 2018.1.00272.S and cycle 8 project 2021.00439.S to capture multiple CO and  $^{13}\text{CO}$  lines to perform the RADEX modeling. Our Band 3 observations on CO  $J=1-0$  (from project 2018.1.00272.S) employ configurations of C43-5, C43-2 and ACA, which cover scales from 870 arcsec down to 0.55 arcsec. The spectral resolution is  $2.54 \text{ km s}^{-1}$ . Our Band 3 observations on  $^{13}\text{CO}$   $J=1-0$  (from project 2021.1.00439.S) employ configurations of C43-4, C43-1 and ACA, which cover scales from 900 arcsec down to 1 arcsec. The spectral resolution is  $2.7 \text{ km s}^{-1}$ . We also observed  $\text{C}^{18}\text{O}$   $J=1-0$  in the same frequency tuning. Our Band 6 observations on CO and  $^{13}\text{CO}$   $J=2-1$  (from project 2021.1.00439.S) employ configurations of C43-4, C43-1 and ACA, which covers spatial scales from 415 arcsec down to 0.26 arcsec. The spectral resolution is  $2.54 \text{ km s}^{-1}$ . We also observed  $\text{C}^{18}\text{O}$   $J=2-1$  in the same spectral tuning. Our Band 7 observations on CO  $J=3-2$  (from project 2021.1.00439.S) employ configurations C43-3 and ACA, which cover spatial scales from 270 arcsec down to 0.37 arcsec. The velocity resolution is  $3.4 \text{ km s}^{-1}$ . A summary of the data information is in Table 1.

We calibrate the raw visibility data with the observatory-supplied calibration scripts and the appropriate version of the CASA pipeline. From the calibrated measurement sets, we extract and image a relevant subset of visibility data for each molecular line using a modified version of the PHANGS–ALMA imaging pipeline (Leroy et al. 2021). Before imaging lines, we performed continuum subtraction by subtracting the 1st-order fit modeling on line-free channels. We then combine the 12m and 7m measurement set together and perform the imaging. The imaging steps generally follow the PHANGS imaging scheme (Leroy et al. 2021). We first run a shallow, multi-scale cleaning to pick up regions with S/N of 4 detection. We then run a deep single-scale cleaning down to the threshold of  $2 \times \text{RMS}$ . The single-scale cleaning is restricted to regions that are picked out in the multi-scale cleaning. For the weighting of the visibility data, we adopt the the *Briggs* method with robustness parameter of 0.5. After the cleaning, we then feather the cleaned image product with TP data and apply the primary beam correction to get final image cubes for each line. We also smooth all the images to the smallest round beam. In the final step, we convert all the image cubes to units of Kelvin (K).

We then perform post-processing steps to homogenize all 5 CO lines. We smooth all five image cubes to the resolution of 150 pc (1.41 arcsec) and match all their

**Table 1.** ALMA CO data products

Lines/Continuum	ALMA	Native	LAS	Velocity	RMS <sub>native</sub>	RMS <sub>150pc</sub>
	Band	Resolution		Resolution		
(1)	(2)	(3)	(4)	(5)	(6)	(7)
CO $J=1-0$	3	0''.84, 90 pc	14'.5, 93 kpc	2.54 km s <sup>-1</sup>	0.09 K	0.05 K
CO $J=2-1$	6	0''.51, 54 pc	6'.9, 44 kpc	2.54 km s <sup>-1</sup>	0.24 K	0.11 K
CO $J=3-2$	7	0''.67, 71 pc	4'.5, 29 kpc	3.4 km s <sup>-1</sup>	0.09 K	0.04 K
<sup>13</sup> CO $J=1-0$	3	1''.41, 150 pc	15', 96 kpc	2.7 km s <sup>-1</sup>	0.04 K	0.04 K
<sup>13</sup> CO $J=2-1$	6	0''.71, 76 pc	6'.9, 44 kpc	5.3 km s <sup>-1</sup>	0.09 K	0.05 K
continuum	7	0''.65, 72 pc	0'.34, 2.2 kpc	–	0.18 mJy/beam	0.4 mJy/beam

Columns: (1) CO spectral lines. (2) Native resolution for the smallest round beam. (3) Largest angular scale. (4) Velocity resolution. (5) Noise of the image cubes at the native resolution (6) Noise of the image cubes after smoothing to the resolution of 150 pc.

spatial grids to the CO  $J=1-0$  line. We then produced a set of moment maps and effective width ( $\sigma_v$ ) maps for all five lines at this common resolution. Specifically, the effective width is measured as the ratio between integrated intensity (moment 0) and peak brightness temperature (moment 8) maps, which is

$$\sigma_v = \frac{I}{\sqrt{2\pi}T_{\text{peak}}} \quad (2)$$

For a perfect Gaussian line profile, the effective width is identical to the traditionally used moment 2 measurements. We adopt this alternative method because it gives a more stable estimate of velocity dispersion within clouds, specifically if two or more clouds are along the same line of sight (see Heyer et al. 2001; Sun et al. 2018, for more details). To make moment maps, we start with generating masks adopting the scheme of the PHANGS-ALMA pipeline, which starts from a high-confidence mask including at least two consecutive channels with S/N above 5 and then expand the mask to include pixels with S/N above 2 for at least two consecutive channels. We run this scheme for each line and combine all the mask together to create a "combo" mask. We then apply this common "combo" mask to all the five line data cubes to make moment maps and their corresponding error maps. We also apply a S/N of 3 cut to the moment 0 maps of each line to exclude noisy pixels in weak line maps. In the final steps, we Nyquist-sample the moment 0 and effective width maps for all the lines to remove the spatial correlation between different pixels. Some representative moment maps are shown in Fig. 1 and 2.

## 2.2. ALMA continuum

We also make the ALMA Band 7 continuum image in order to calculate the dust and gas mass. After the calibration of the Band 7 data, we use the PHANGS-ALMA pipeline (Leroy et al. 2021) to combine the 12m and 7m measurement sets and extract the line-free channels

from the combined measurement set for the continuum imaging. We also collapse each spectral window into a single channel in order to speed up the continuum imaging process. We then use the `auto-multithresh` algorithm to clean the continuum data down to threshold of  $2 \times \text{RMS}$  (RMS of  $\sim 0.18$  mJy/beam). After imaging, we smooth the dust continuum map to the resolution of 150 pc and regrid the map to the nyquist-sampled CO images.

## 2.3. Spitzer Data

We use the *Spitzer* 3.6  $\mu\text{m}$  (Program 10136) and 4.5  $\mu\text{m}$  (Program 61068) data to calculate the stellar mass surface density of the Antennae at kpc scale. We reproject both image to match the pixel grids of CO 150 pc resolution moment maps. We then calculate the stellar mass for each pixel with the equation (Eskew et al. 2012)

$$M_{\star} = 10^{5.65} F_{3.6}^{2.85} F_{4.5}^{-1.85} (D/0.05)^2 [\text{M}_{\odot}], \quad (3)$$

where  $F_{3.6}$  and  $F_{4.5}$  are the flux at 3.6 and 4.5  $\mu\text{m}$ , respectively and  $D$  is the luminosity distance in Mpc. We then calculate the stellar surface density by dividing the pixel area using equation

$$\Sigma_{\star} = M_{\star}/(150 \text{ pc})^2 [\text{M}_{\odot} \text{ pc}^{-2}] \quad (4)$$

At the final step, we regrid our calculated stellar surface density map to the grid of 1 kpc resolution nyquist sampled CO  $J=1-0$  moment 0 map.

## 3. RADEX MODELING

### 3.1. General Modeling Procedure

We adapt the code<sup>1</sup> from Teng et al. (2022) to perform non-LTE radiative transfer modeling for each pixel

<sup>1</sup> <https://github.com/ElthaTeng/multiline-bayesian-modeling>

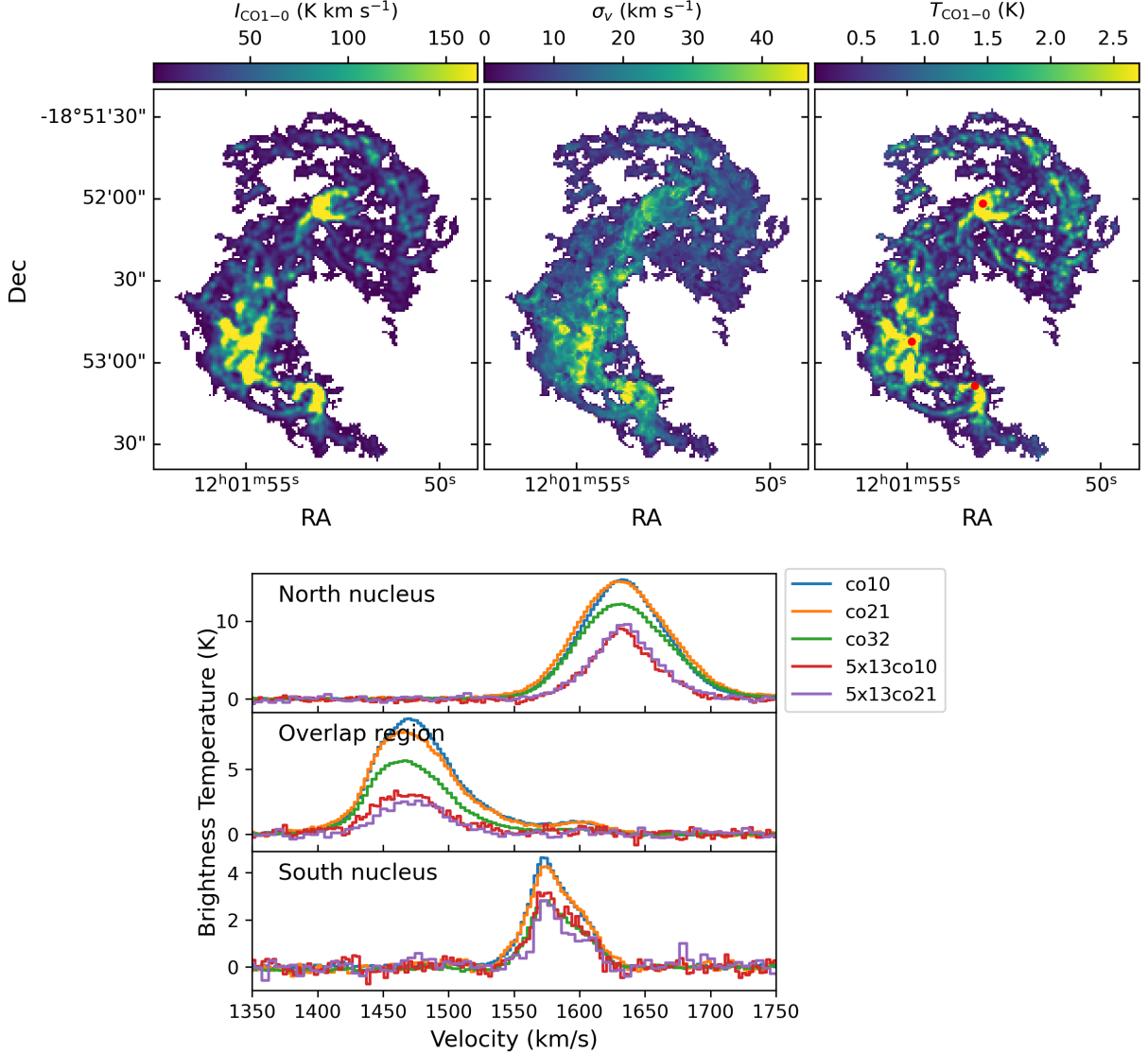


**Figure 1.** (Top) Integrated intensity, velocity dispersion and peak brightness temperature of the CO  $J=1-0$  observations at 150 pc resolution. The three red points in the map of peak brightness temperature map indicate three representative pixels in the north nucleus, overlap region and south nucleus. (Bottom) CO and  $^{13}\text{CO}$  spectra for the three representative pixels marked in the top map.

with all five CO and  $^{13}\text{CO}$  lines detected at 150 pc. We briefly summarize the code and our adaptation below (please refer to Teng et al. 2022; Teng et al. 2023, for more details). This code runs RADEX (Van Der Tak et al. 2007) modeling, which assumes a homogeneous medium and uses radiative transfer equations based on the escape probability formalism to find a converged solution for the excitation temperature and level population for each molecular line transition. We adopt the one-component RADEX modeling to generate 5D grids of integrated line intensities for the five lines under combinations of varying  $\text{H}_2$  volume density ( $n$ ), kinetic temperature ( $T_{\text{kin}}$ ), CO column density ( $N_{\text{CO}}$ ),  $\text{CO}/^{13}\text{CO}$

abundance ratio ( $X_{12/13}$ ) and beam filling factor ( $\Phi_{\text{bf}}$ ). Since RADEX modeling only cares about  $N_{\text{CO}}/\Delta v$  instead of  $N_{\text{CO}}$  alone, we instead sample CO column density per  $15 \text{ km s}^{-1}$  ( $N_{\text{CO}} \times \frac{15 \text{ km s}^{-1}}{\Delta v}$ ). The  $15 \text{ km s}^{-1}$  is the fiducial value used in Teng et al. (2023); Teng et al. (2024). Later we will rescale this value to the real CO column density based on the measured  $\Delta v$  in CO  $J=1-0$  velocity dispersion map ( $\Delta v = 2.35\sigma_v$ ). In the modeling, we assume the same  $\Phi_{\text{bf}}$  for all 5 lines. We also assume the  $\text{CO}/\text{H}_2$  abundance ratio ( $x_{\text{co}}$ ) of  $3 \times 10^{-4}$ . We will discuss our  $x_{\text{CO}}$  choice in Section 5.2. Our input parameters are summarized in Table 2.

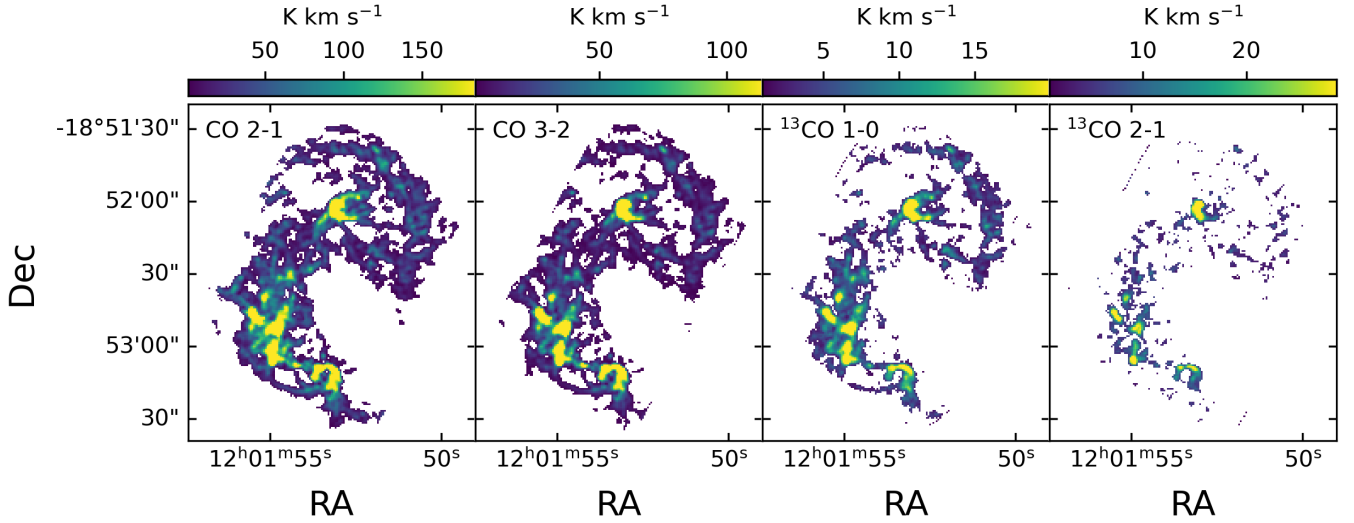


**Figure 2.** Integrated intensity maps for CO  $J=2-1$ ,  $3-2$  and  $^{13}\text{CO } J=1-0$  and  $2-1$  lines at 150 pc resolution. Pixels with S/N smaller than 3 are masked (see text).

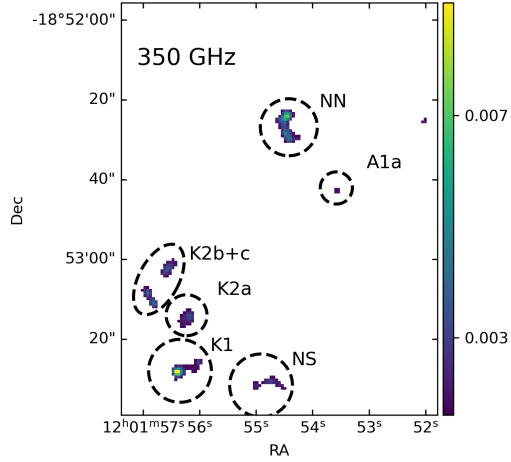


**Figure 3.** 350 GHz dust continuum map of the Antennae. Pixels with S/N < 4 are masked. Dashed circles corresponds to knots in the Herschel  $70 \mu\text{m}$  map identified in Klaas et al. (2010).

**Table 2.** RADEX Input Parameters

Parameter	Range	Step
$\log(n)$ ( $\text{cm}^{-3}$ )	2 – 5.1	0.2
$\log(T_{\text{kin}})$ (K)	1 – 2.4	0.1
$\log(N_{\text{CO}} \times \frac{15\text{kms}^{-1}}{\Delta v})$ ( $\text{cm}^{-2}$ )	16 – 21	0.2
$X_{12/13}$	10 – 400	10
$\Phi_{\text{bf}}$	0.05 – 1	0.05
$[\text{CO}]/[\text{H}_2]$	$3 \times 10^{-4}$	–

We then follow the Bayesian likelihood analyses in Teng et al. (2022) to characterize the probability density function (PDF) for the five varying parameters. For each pixel, the code calculates the  $\chi^2$  by comparing the

modeled line intensities with the measured line intensities. Note that in Teng et al. (2022), they compare modeled and measured integrated line intensities. While they assumed a fixed velocity FWHM that is representative of their observed region, this may introduce the issue that the fixed velocity FWHM ( $15 \text{ km s}^{-1}$ ) in the modeling is inconsistent with varying velocity FWHMs measured for different pixels in the observations (see Appendix B in Teng et al. 2023, for further discussion). Since our modeled intensity corresponds to linewidth of  $15 \text{ km s}^{-1}$ , we need to rescale modeled intensity by multiplying the ratio of measured linewidth to the fixed linewidth of  $15 \text{ km s}^{-1}$  for each pixel. Then we calculate the  $\chi^2$  matrix as

$$\chi^2(\vec{\theta}) = \sum_{i=1}^{N=5} \frac{I_i^{\text{mod, scaled}}(\vec{\theta}) - I_i^{\text{obs}}}{\sigma_i^2} \quad (5)$$

where  $\vec{\theta}$  represents each modeled parameter set of  $(n_{\text{H}_2}, T_{\text{kin}}, N_{\text{CO}}/\Delta v, X_{12/13}, \Phi_{\text{bf}})$ ,  $I_i^{\text{mod, scaled}} = I_i^{\text{mod}} \frac{\Delta v}{15\text{kms}^{-1}}$  represents the scaled modeled integrated intensity for each line and  $I_i^{\text{obs}}$  represents the integrated intensities from observations,  $\sigma_i$  the measurement uncertainty for  $I_i^{\text{obs}}$  of each line and  $N$  specifies the number of lines used for the modeling. For each pixel value, we calculate the posterior probability distribution function across the 5D model parameter space as

$$P(\vec{\theta}|\vec{I}_{\text{obs}}) = \frac{1}{Q} \exp(-\chi^2/2) \quad (6)$$

where  $Q^2 = (2\pi)^5 \prod_i \sigma_i^2$  is the normalization coefficient. From the 5D distribution, we can calculate the 'Best-fit' set of modeled parameters with maximal  $P(\vec{\theta}|\vec{I}_{\text{obs}})$ . We can also calculate the marginalized 1D probability

**Table 3.** Solutions for the Modeled Parameter

Solution	Condition
Bestfit	$P(\vec{\theta}_{\text{Bestfit}} \vec{I}_{\text{obs}}) = \max P(\vec{\theta} \vec{I}_{\text{obs}})$
1DMax	$P(\theta_{i,1\text{DMax}} \vec{I}_{\text{obs}}) = \max P(\theta_i \vec{I}_{\text{obs}})$
Neg1Sig	$\int^{\theta_{i,\text{Neg1Sig}}} d\theta_i P(\theta_i \vec{I}_{\text{obs}}) = 0.16$
Median	$\int^{\theta_{i,\text{Median}}} d\theta_i P(\theta_i \vec{I}_{\text{obs}}) = 0.5$
Pos1Sig	$\int^{\theta_{i,\text{Pos1Sig}}} d\theta_i P(\theta_i \vec{I}_{\text{obs}}) = 0.84$

distribution for each individual modeled parameter by integrating the 5D  $P(\vec{\theta}|\vec{I}_{\text{obs}})$  over the rest of parameter space. The equation for the 1D marginalized distribution is

$$P(\theta_i|\vec{I}_{\text{obs}}) = \int \cdots \int_{j \neq i} d\theta_j P(\vec{\theta}|\vec{I}_{\text{obs}}) \quad (7)$$

where  $\theta_i$  is the one modeled parameter that we want to calculate the 1D marginalized distribution and  $\theta_j$  are the rest of modeled parameters. From the 1D marginalized distribution, we can calculate the '1DMax' solution for each modeled parameter with largest  $P(\theta_i|\vec{I}_{\text{obs}})$ . We can also calculate the 16<sup>th</sup>, 50<sup>th</sup> and 84<sup>th</sup> percentile of the cumulative 1D distributions as  $-1\sigma$ , median and  $+1\sigma$  values. We have summarized the statistical quantities from our modeling in Table 3.

We show the 1D and 2D probability distribution for each modeled quantity in Fig. 4 for one of the pixels in north nucleus (marked as red dot in Fig. 1). For most of quantities, the median of the 1D probability distribution corresponds well with the '1DMax' value of the distribution, which suggests that our modeling recovers the most probable solution. One exception is  $X_{12/13}$ , which has double peaks in its 1D distribution. This is a common behavior for most of our pixels, which suggests that the  $X_{12/13}$  value is less well constrained. Therefore, for all of the modeled physical quantities except for  $X_{12/13}$ , we adopt the median value as our modeled solution. For  $X_{12/13}$ , we instead use '1DMax' value as the modeled solution.

### 3.2. Modeling of CO-to-H<sub>2</sub> conversion factor

The CO-to-H<sub>2</sub> conversion factor  $\alpha_{\text{CO}}$  is calculated (Teng et al. 2022) as

$$\begin{aligned} \alpha_{\text{CO}} &= \frac{\Sigma_{\text{mol}}}{I_{\text{CO}(1-0)}} \left[ \frac{\text{M}_{\odot}}{\text{K km s}^{-1}} \right] \\ &= \frac{1.36 m_{\text{H}_2} N_{\text{CO}} \Phi_{\text{bf}}}{x_{\text{co}} I_{\text{CO}(1-0)}} \\ &= \frac{1}{4.5 \times 10^{19}} \frac{N_{\text{CO}} [\text{cm}^{-2}] \Phi_{\text{bf}}}{x_{\text{co}} I_{\text{CO}(1-0)} [\text{K km s}^{-1}]}, \end{aligned} \quad (8)$$

where  $x_{\text{co}}$  is the [CO]/[H<sub>2</sub>] abundance ratio. This equation has applied for the correction coefficient of 1.36

for helium contribution. This equation shows the key modeling parameters to constrain  $\alpha_{\text{CO}}$  are the CO column density  $N_{\text{CO}}$ , beam filling factor  $\Phi_{\text{bf}}$  and [CO]/[H<sub>2</sub>] abundance ratio. Therefore, we can calculate  $\alpha_{\text{CO}}$  1D distribution by summing up all the probabilities of parameters in 5D space that yield a given  $\alpha_{\text{CO}}$  value, which is

$$\begin{aligned} P_{\text{biased}}(\alpha_{\text{CO}}|\vec{I}_{\text{obs}}) &= P_{\text{biased}}\left(\frac{N_{\text{CO}} \Phi_{\text{bf}}}{x_{\text{co}} I_{\text{CO}(1-0)}^{\text{mod, scaled}}}|\vec{I}_{\text{obs}}\right) \\ &= \int_{f(\vec{\theta})=\alpha_{\text{CO}}} d\vec{\theta} P(\vec{\theta}|\vec{I}_{\text{obs}}) \end{aligned} \quad (9)$$

where  $f(\vec{\theta}) \equiv \frac{N_{\text{CO}} \Phi_{\text{bf}}}{x_{\text{co}} I_{\text{CO}(1-0)}^{\text{mod, scaled}}}$ . However, we need to note that  $\alpha_{\text{CO}}$  is not uniformly sampled in our 5D parameter space. To get the unbiased PDF, we calculate the normalized ratio of our biased  $\alpha_{\text{CO}}$  probability to the  $\alpha_{\text{CO}}$  prior probability in our sampling space, which is

$$P(\alpha_{\text{CO}}|\vec{I}_{\text{obs}}) = \left[ \frac{P_{\text{biased}}(\alpha_{\text{CO}}|\vec{I}_{\text{obs}})}{P_{\text{prior}}(\alpha_{\text{CO}})} \right]_{\text{norm}} \quad (10)$$

An example on the 3  $\alpha_{\text{CO}}$  PDFs for one pixel is shown in Fig. 5.

We find that some pixels have extremely small  $\alpha_{\text{CO}}$  values. As shown in Fig. 5,  $\alpha_{\text{CO}}$  values below 0.1 are not well sampled and the prior distribution has a huge drop below this threshold. Therefore, we exclude the pixels with median  $\alpha_{\text{CO}}$  value below 0.1. We also exclude  $\alpha_{\text{CO}}$  with larger uncertainties ( $\alpha_{\text{CO, pos1sig}}/\alpha_{\text{CO, neg1sig}} < 16$ , which means uncertainty within a factor of 4). We further exclude pixels with 1dMax values of modeled quantities at the edge of our parameter space. Specifically, we apply the selection criterion to mask out pixels with  $X_{12/13, 1\text{DMax}} \leq 30$ ,  $\log n_{\text{H}_2, 1\text{DMax}} \geq 4.9$ ,  $\log(N_{\text{CO}, 1\text{DMax}} \times \frac{15 \text{ km s}^{-1}}{\Delta v}) \leq 16.1$  and  $\log(T_{\text{kin}, 1\text{DMax}}) < 1.1$ . We also exclude pixels with  $\chi^2$  value greater than 10. After applying all the selection criterion, we have 508 pixels with good RADEX model constraint.

Note that our derived  $\alpha_{\text{CO}}$  is dependent on our assumed  $x_{\text{CO}}$  value. In Section 5.2, we will discuss reasonable  $x_{\text{CO}}$  choice. The equation to convert our derived  $\alpha_{\text{CO}}$  to the real  $\alpha_{\text{CO}}$  with known  $x_{\text{CO}}$  value is

$$\alpha_{\text{CO}}^{\text{real}} = \frac{3 \times 10^{-4}}{x_{\text{CO}}} \alpha_{\text{CO}}^{\text{derived}} \quad (11)$$

## 4. GAS PHYSICAL PROPERTIES AT GMC SCALES

### 4.1. Line Ratios

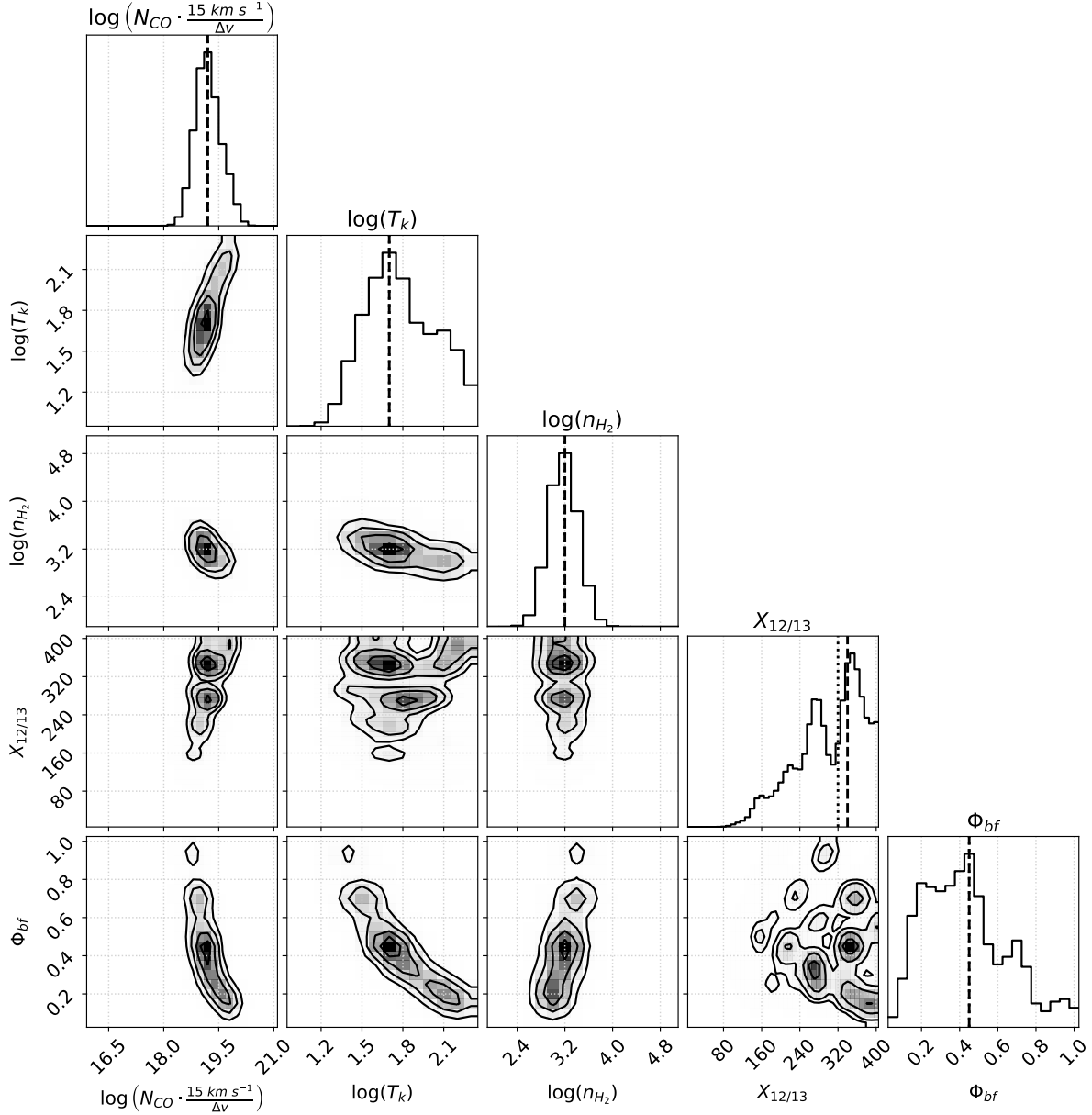


**Figure 4.** Corner plot of modeled RADEX physical properties for the north nucleus pixel (Fig. 1). From the left to right is the scaled CO column density ( $\text{cm}^{-2}$ ), kinetic temperature (K), hydrogen volume density ( $\text{cm}^{-3}$ ),  $[\text{CO}]/[^{13}\text{CO}]$  abundance ratio and beam filling factor. The dashed and dotted lines mark the maximal and median of the 1D distribution for each quantity.

The brightness temperature ratios of different lines can be used to probe differences in molecular gas properties among different regions. The line ratio maps are shown in Fig. 6 and 7. For all the ratio maps, we apply a  $S/N > 3$  cut to the  $^{13}\text{CO}$   $J=1-0$  and  $2-1$  moment 0 maps to exclude pixels with  $^{13}\text{CO}$  non-detections.

The CO  $J=3-2/1-0$  and CO  $J=2-1/1-0$  ratios are indicators of the CO excitation, which is directly related to the molecular gas temperature and/or volume density (Leroy et al. 2017). Fig. 6 shows the two ratio maps along with their dependencies on CO  $J=1-0$  brightness

temperature. We can see that the CO  $J=2-1/1-0$  ratio is generally uniform with values close to 1 across the entire molecular gas detected region. This uniformity suggests that both CO  $J=1-0$  and  $2-1$  are thermally excited, which generally holds for warm, dense and CO optically thick environments (Salak et al. 2019) that are typical in starburst systems (e.g. Sliwa et al. 2017b). Simulations also predict that the low- $J$  CO lines are mostly thermalized for typical starburst mergers (e.g. Bournaud et al. 2015). The CO  $J=2-1/1-0$  ratio in the Antennae is also larger than those of normal spiral galaxies of  $\sim$



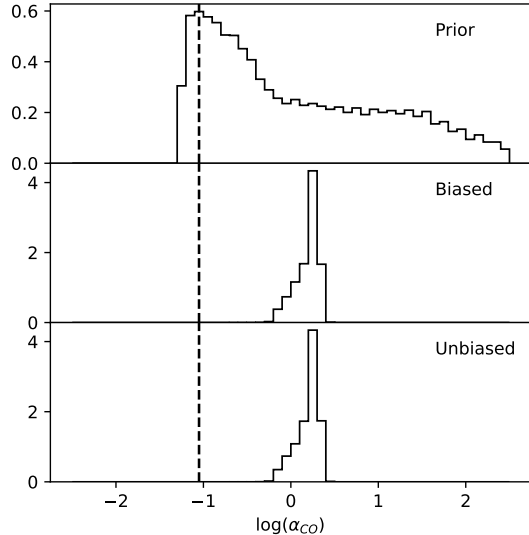


**Figure 5.** Marginalized  $\alpha_{\text{CO}}$  distribution for the north nucleus pixel (Fig. 1). (*Top*) The prior distribution of  $\alpha_{\text{CO}}$  calculated by attributing uniform weighting to every set of parameters. (*Middle*) The histogram of  $\alpha_{\text{CO}}$  posterior distribution without sampling bias correction. (*Bottom*) The histogram of  $\alpha_{\text{CO}}$  posterior distribution after correcting for the sampling bias. To the right of the dashed line is where the  $\alpha_{\text{CO}}$  is not well sampled in our parameter space.

0.7 (Leroy et al. 2021), which is the commonly used ratio value to convert between CO  $J=2-1$  and CO  $J=1-0$  brightness temperature. On the other hand, this ratio value is consistent with what measured in starburst U/LIRGs (Montoya Arroyave et al. 2023). Since most GMC observations for starburst mergers (e.g. Brunetti et al. 2020; Brunetti & Wilson 2022) are done using CO  $J=2-1$  line due to its higher resolution and sensitivity, it is important to assume an appropriate CO  $J=2-1/1-0$  ratio for the gas mass calculation. Our study suggests that a typical starburst merger should have CO  $J=2-1/1-0$  ratio values close to 1 instead of the commonly adopted 0.7.

On the other hand, the CO  $J=3-2/1-0$  ratio shows a clear spatial variation among different regions. In particular, the ratio is high in the gas concentrated regions, such as the two nuclei and the overlap region. We can also see a clear trend that the CO  $J=3-2/1-0$  ratio increases as the CO  $J=1-0$  intensity (or gas surface density) increases (Fig. 6, lower-right panel). This trend suggests that gas in these gas-concentrated regions is either denser and/or warmer than the rest of regions. The average CO  $J=3-2/1-0$  ratio is  $\sim 0.4 - 0.7$  (Fig. 6, lower right panel), which is much higher than those of normal spiral galaxies of  $\sim 0.3$  (e.g. NGLS survey, Wilson et al. 2012; Leroy et al. 2022). Instead, this ratio value

is close to that of the centers of normal spiral galaxies of  $\sim 0.8$ , such as M 31 (Li et al. 2020) and M 51 (Vlahakis et al. 2013), which suggests that the physical states of molecular gas in starburst systems are similar to that of central region of normal spiral galaxies. Compared to starburst U/LIRGs, our measured ratio is also slightly higher. Wilson et al. (2008) measured an average CO  $J=3-2/1-0$  ratio of 0.5 for a large sample of U/LIRGs, which generally have higher molecular gas and SFR surface density than the Antennae. A possible explanation is that we are probing much denser gas at GMC scales with  $^{13}\text{CO}$  detections while the ratio measured in Wilson et al. (2008) is at kpc scales which can include a lot of diffuse gas where CO  $J=3-2$  is less excited. We also note there is a discrepancy between our measured CO  $J=3-2/1-0$  ratio and the literature values of 0.25 (Ueda et al. 2012; Bigiel et al. 2015) for the Antennae, which is probably due to the same resolution effect.

We also make  $^{13}\text{CO}/\text{CO}$   $J=1-0$  and  $^{13}\text{CO}/\text{CO}$   $J=2-1$  ratio maps for the Antennae (Fig. 7), which can be used to probe the  $[^{13}\text{CO}]/[\text{CO}]$  abundance ratio and the optical depth (e.g. Jiménez-Donaire et al. 2017). Due to CO being optically thick, it is hard to disentangle all these factors without comprehensive LVG modeling. To demonstrate this degeneracy, we first consider a simple case where both CO and  $^{13}\text{CO}$  lines are thermally excited to the kinetic temperature, which should not be far off from the real situation as discussed above. We use CO and  $^{13}\text{CO}$   $J=1-0$  lines for the demonstration but we would expect this also applies to CO and  $^{13}\text{CO}$   $J=2-1$  lines. Under the local thermal equilibrium (LTE) condition, we would expect the  $^{13}\text{CO}/\text{CO}$  line ratio to be

$$\begin{aligned}
 R_{^{13}\text{CO}/\text{CO}1-0} &= \frac{T_{^{13}\text{CO}1-0}^{\text{peak}}}{T_{\text{CO}1-0}^{\text{peak}}} \\
 &= \frac{\Phi_{\text{bf}} T_{\text{kin}} [1 - \exp(-\tau_{^{13}\text{CO}1-0})]}{\Phi_{\text{bf}} T_{\text{kin}} [1 - \exp(-\tau_{\text{CO}1-0})]} \\
 &\approx \tau_{^{13}\text{CO}1-0}, \quad (\tau_{^{13}\text{CO}1-0} \ll 1 \ll \tau_{\text{CO}1-0})
 \end{aligned} \tag{12}$$

Since the  $^{13}\text{CO}$   $J=1-0$  optical depth can be simply expressed as the CO  $J=1-0$  optical depth divided by the  $[\text{CO}]/[^{13}\text{CO}]$  abundance ratio ( $X_{12/13}$ ), the  $^{13}\text{CO}/\text{CO}$   $J=1-0$  ratio can be further expressed as

$$R_{^{13}\text{CO}/\text{CO}1-0} \approx \tau_{^{13}\text{CO}1-0} = \tau_{\text{CO}1-0}/X_{12/13} \tag{13}$$

Therefore, if we observe a higher  $R_{^{13}\text{CO}/\text{CO}1-0}$ , it can be either due to higher CO optical depth (and hence higher column density) and/or lower  $X_{12/13}$  abundance ratio. We need to note that our simple derivation assumes both CO and  $^{13}\text{CO}$   $J=1-0$  lines are thermally excited and share the same beam filling factor  $\Phi_{\text{bf}}$  and the

same linewidth  $\Delta v$ . In the real case, since CO  $J=1-0$  is generally optically thick while  $^{13}\text{CO } J=1-0$  is optically thin, the effective critical density of CO  $J=1-0$  is lower than that of  $^{13}\text{CO } J=1-0$  due to the line trapping effects. This will lead to lower beam filling factor and excitation temperature for  $^{13}\text{CO } J=1-0$  line and hence lower  $R_{^{13}\text{CO}/\text{CO}1-0}$  value, specifically for lower-density regions (Jiménez-Donaire et al. 2017, see detailed discussion in). Therefore, we would also expect higher  $R_{^{13}\text{CO}/\text{CO}1-0}$  in regions with higher gas volume density.

We can see both  $R_{^{13}\text{CO}/\text{CO}1-0}$  and  $R_{^{13}\text{CO}/\text{CO}2-1}$  have similar values of  $\sim 0.1$ . This ratio is similar to the typical  $R_{^{13}\text{CO}/\text{CO}1-0}$  ratio of 0.1 for normal spiral galaxies (e.g. Cormier et al. 2018). On the other hand, this ratio is much higher than typical ratio of starburst U/LIRGs ( $\sim 0.02$  Brown & Wilson 2019). It is still an open question about what cause the extremely low  $R_{^{13}\text{CO}/\text{CO}}$  ratio in typical U/LIRGs. While RADEX modeling suggests lots of U/LIRGs have extremely high  $X_{12/13}$  of  $\sim 100$  (Matsushita et al. 2009; Sliwa et al. 2017a), some exceptions have been found with low  $X_{12/13}$  solution (e.g. Arp 55, Sliwa et al. 2017b) but also low  $^{13}\text{CO}/\text{CO}$  ratios ( $\sim 0.03$ ). An alternative scenario (Papadopoulos et al. 2012) is that the stellar feedback can increase velocity linewidth of molecular line emissions and hence reduce the CO and  $^{13}\text{CO}$  optical depth, and then reduce the  $^{13}\text{CO}/\text{CO}$  ratio (Eq. 13). Since the Antennae has normal  $^{13}\text{CO}/\text{CO}$  line ratios as normal spiral galaxies but yet higher  $X_{12/13}$  values ( $\sim 200$ , Section 4.2) than normal spiral galaxies ( $\sim 60$  Jiménez-Donaire et al. 2017) but comparable to U/LIRGs, it is possible the normal  $^{13}\text{CO}/\text{CO}$  ratio is due to the combined effect of high optical depth and high  $X_{12/13}$  values in the Antennae. We note that the Antennae has comparable molecular gas mass but less total SFR than typical U/LIRGs (e.g. NGC 3256 Brunetti 2022), which might suggest that stellar feedback might not yet be effective to reduce the molecular gas optical depth in the Antennae.

We also note that both  $R_{^{13}\text{CO}/\text{CO}1-0}$  and  $R_{^{13}\text{CO}/\text{CO}2-1}$  decrease as the CO intensity increases until  $I_{\text{CO}(1-0)} \approx 200 \text{ K kms}^{-1}$  (Fig. 7, upper and lower right panel). Under LTE condition, this indicates that regions with higher CO luminosity actually have lower  $^{13}\text{CO}$  optical depth, which could be caused by larger velocity dispersion in these regions (see detailed discussion in Section 5.1.3). An alternative is that the LTE condition is not satisfied and hence the  $R_{^{13}\text{CO}/\text{CO}}$  ratio no longer trace the  $^{13}\text{CO}$  optical depth (see discussion in Section 4.2).

#### 4.2. Modeling results and their connection to the line ratios

We show the maps of our derived physical quantities in Fig. 8. We can see that most quantities show clear spatial variations among different regions. If we use the CO column density map as a guide, we can see that regions with higher gas surface densities, such as the two nuclei and the overlap region, generally have higher kinetic temperatures, beam filling factors and  $[\text{CO}]/[^{13}\text{CO}]$  abundance ratios. On the other hand, the volume density distributions are more uniform throughout the entire galaxy. We note that we only include pixels with  $^{13}\text{CO}$  line detections for RADEX modeling. Therefore, we would expect these regions to have higher volume densities than those with only CO detections (Jiménez-Donaire et al. 2017).

The spatial variations of these quantities are also closely related to the line ratio maps. We can see that the kinetic temperature map looks similar to the CO  $J=3-2/1-0$  ratio maps. This is consistent with our expectations that CO  $J=3-2$  is more excited in warmer regions. As we previously discussed, the higher CO  $J=3-2/1-0$  ratio could either be caused by higher temperature or density. Since the volume density does not have as much spatial variation as the kinetic temperature, it seems the major driver for the CO  $J=3-2/1-0$  ratio variation is temperature. We have also discussed that the CO  $J=2-1/1-0$  ratio map looks uniformly close to 1, which suggests both lines are thermalized. Under this condition, we would expect the excitation temperature of these two lines are equal to the kinetic temperature. In Fig. 9 (upper left and middle panel), we compare the excitation temperature of CO  $J=2-1$  and  $1-0$  lines with the kinetic temperature. We can see both lines have excitation temperatures close to the one-to-one lines, which further confirms they are thermalized. Simulations (e.g. Hu et al. 2022) suggest that the LTE conditions is generally satisfied when kinetic temperature is above 10 K and volume density above  $10^3 \text{ cm}^{-3}$ . As we can see from the temperature and volume density maps (Fig. 8), most of regions satisfy this condition.

On the other hand, most  $^{13}\text{CO } J=1-0$  emission is not thermally excited, hence has excitation temperature lower than the kinetic temperature. However, we expect that most regions should have volume density above the  $^{13}\text{CO } J=1-0$  critical density ( $650 \text{ cm}^{-3}$ , Jiménez-Donaire et al. 2017) and hence be thermally excited as CO  $J=1-0$ . We note that in our model, we assume  $^{13}\text{CO } J=1-0$  has the same beam filling factor as the CO  $J=1-0$  emission. In reality,  $^{13}\text{CO } J=1-0$  might have smaller beam filling factor compared to CO  $J=1-0$  as it mostly come from denser regions. In this case, we might overestimate the actual size of the  $^{13}\text{CO } J=1-0$  emission and hence underestimate the actual exci-

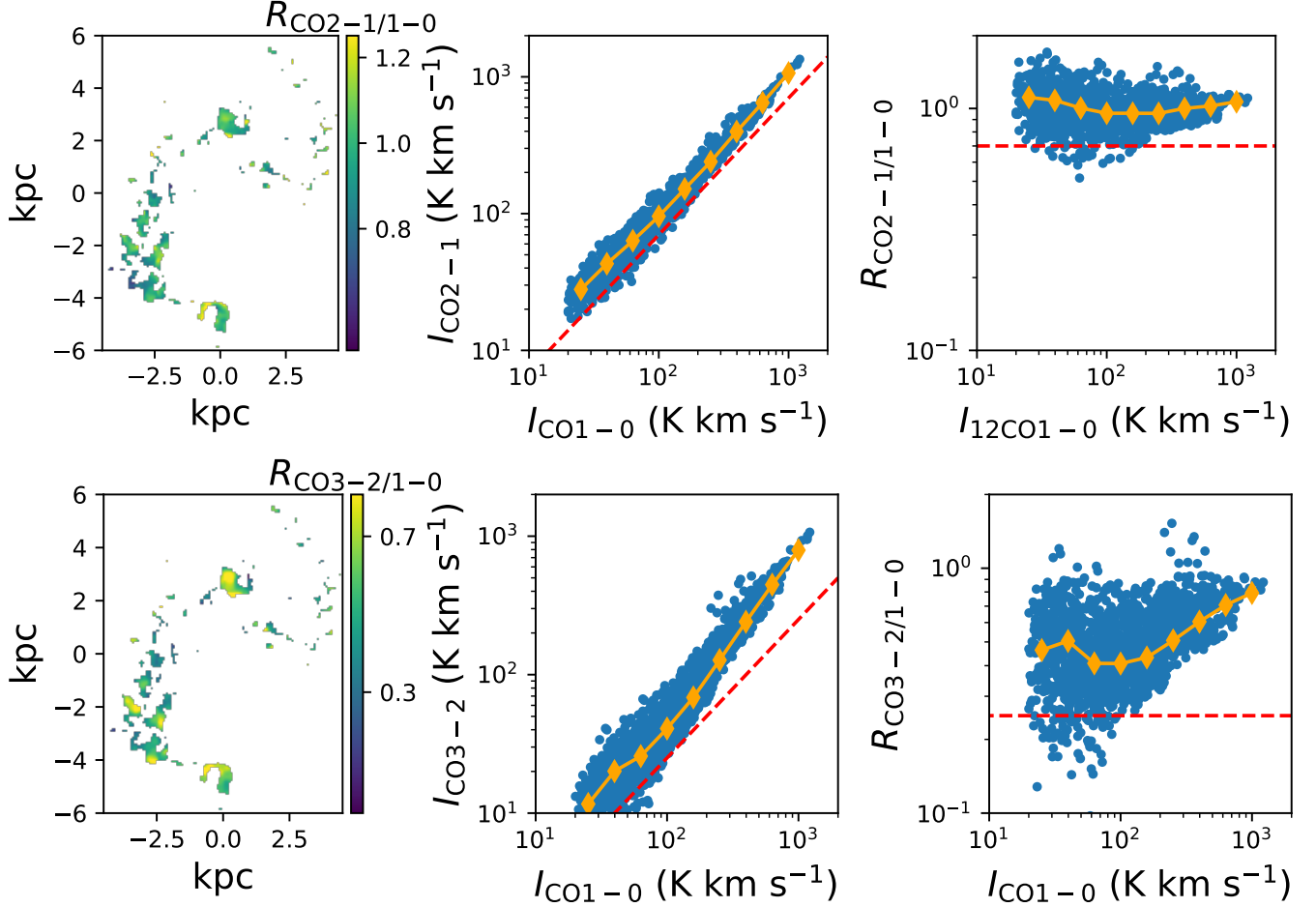


**Figure 6.** Line ratios of (*upper*) CO 2-1/1-0 and (*lower*) CO 3-2/1-0. Orange diamonds specify the median for each CO 1-0 bin. The red dashed lines are the literature ratio values for normal spiral galaxies ( $R_{\text{CO}2-1/1-0} = 0.7$  and  $R_{\text{CO}3-2/1-0} = 0.25$ , Sun et al. 2018). We can see the line ratios in the Antennae are significantly higher than the literature values, which could be due to higher temperature or density of GMCs in starburst systems. The  $R_{\text{CO}2-1/1-0}$  values in the Antennae are uniformly close to 1, which suggests both CO  $J=2-1$  and 1-0 are thermally excited. On the other hand,  $R_{\text{CO}3-2/1-0}$  is significantly higher for regions with higher surface density, which could be either due to high gas temperature and/or volume density in these regions.

tation temperature of  $^{13}\text{CO } J=1-0$  emission. As we have discussed before, under LTE conditions, we would expect  $^{13}\text{CO}/\text{CO } J=1-0$  ratio to be equivalent to the  $^{13}\text{CO } J=1-0$  optical depth. As shown in the lower-left panel of Fig. 9, when LTE condition holds for  $^{13}\text{CO } J=1-0$  ( $T_{\text{ex}}(^{13}\text{CO}1-0) \approx T_{\text{ex}}(\text{CO}1-0)$ ), we see good 1-to-1 correspondence between the ratio and the optical depth. However, since most regions have  $^{13}\text{CO } J=1-0$  emission subthermally excited according to our modeling, we can see that the ratio in those regions is generally smaller than the actual  $^{13}\text{CO } J=1-0$  optical depth. As we have discussed in Section 4.1, the two major drivers for  $^{13}\text{CO}/\text{CO } J=1-0$  ratio variation are the CO  $J=1-0$  optical depth and  $X_{12/13}$  abundance ratio. Since  $^{13}\text{CO } J=1-0$  might not satisfy LTE conditions, we test if the  $^{13}\text{CO}/\text{CO } J=1-0$  ratio are still affected by

those two factors using our RADEX modeling results. As shown in bottom middle and left panel of Fig. 9, our RADEX modeling results suggest that  $R_{^{13}\text{CO}/\text{CO}1-0}$  still has strong correlations with both quantities.

We also note that there is a clear spatial variation of  $X_{12/13}$  that corresponds well with  $T_{\text{kin}}$  and  $N_{\text{CO}}$  variation (Fig. 8). Regions with higher CO column density and kinetic temperature generally have higher  $X_{12/13}$ . In theory, the high  $X_{12/13}$  value could be caused by starburst activity that generates large amounts of  $^{12}\text{C}$  at short timescales ( $\sim 10$  Myr Vigroux et al. 1976) by massive stars while  $^{13}\text{C}$  will only be released by intermediate-mass stars after  $\sim 1$  Gyr. This scenario is consistent with our expectation since regions with higher gas temperature and surface densities are generally where starburst events happen. In Section 4.1,

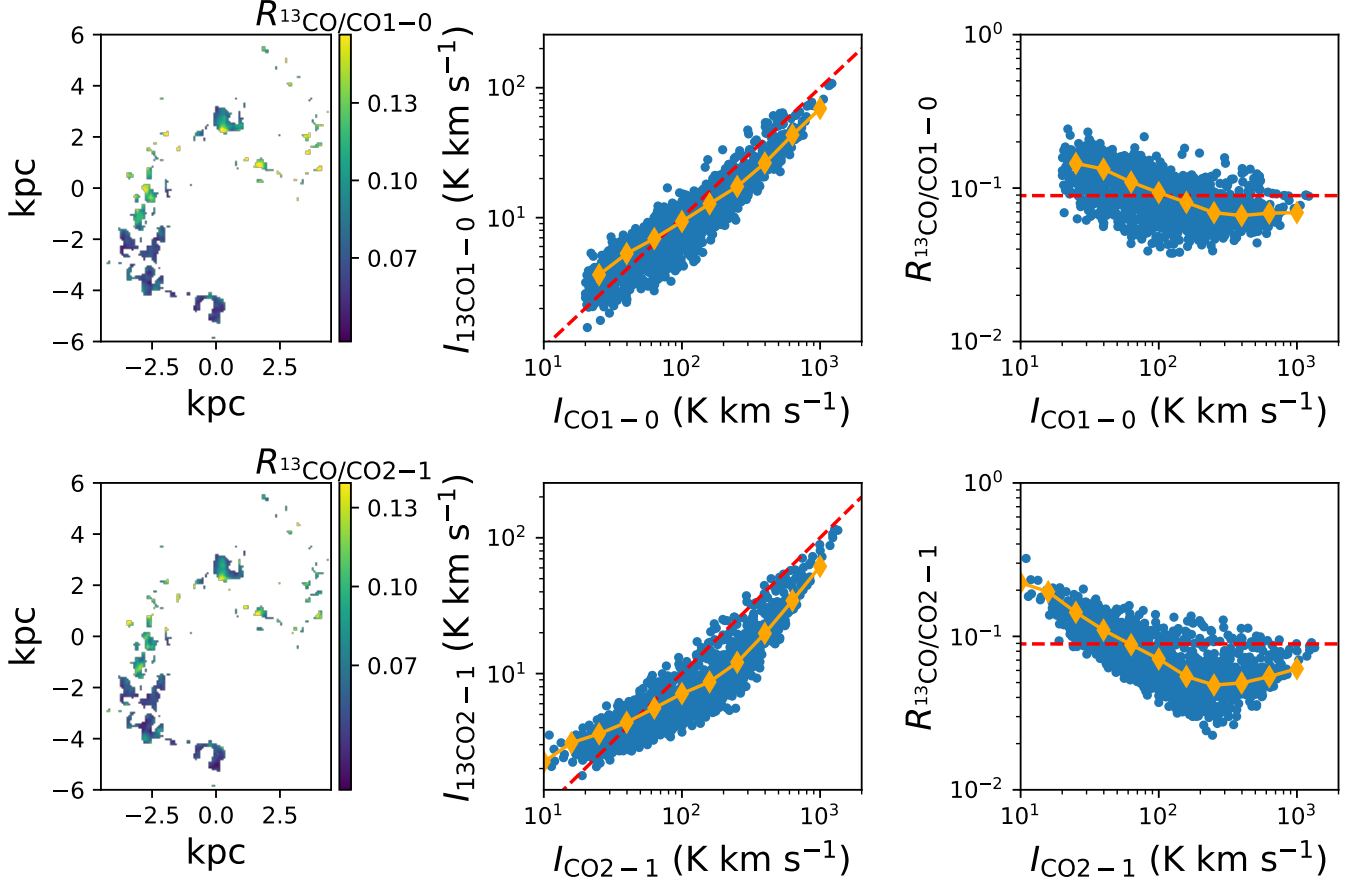


**Figure 7.** Line ratios of  $^{13}\text{CO}/\text{CO}$  1-0 (*upper*) and 2-1 (*lower*). The red dashed lines are the literature ratio values ( $R_{^{13}\text{CO}/\text{CO}1-0} = 0.09$  Cormier et al. 2018). We can see that both  $R_{^{13}\text{CO}/\text{CO}1-0}$  and  $R_{^{13}\text{CO}/\text{CO}2-1}$  have a significant anti-correlation with CO  $J=1-0$  and 2-1 intensity for CO intensities smaller than  $100 \text{ K km s}^{-1}$ . This could either be due to low optical depth of CO or high  $X_{12/13}$  abundance ratio in high surface density region (see text for detailed discussion).

we have also discussed the negative correlation between  $R_{^{13}\text{CO}/\text{CO}1-0}$  and CO  $J=1-0$  intensity. The low  $R_{^{13}\text{CO}/\text{CO}1-0}$  in high surface density regions could be potentially due to high  $X_{12/13}$  in these regions. We also find most regions have  $X_{12/13}$  values between 100 – 300. This value is more similar to the  $X_{12/13}$  in starburst mergers (125 in Arp 220, 250 in NGC 2623 Sliwa & Downes 2017; Sliwa et al. 2017b) and significantly higher than that in solar neighborhood and normal disk galaxies of  $\sim 70$  (e.g. Langer & Penzias 1990; Milam et al. 2005). This is also consistent with the scenario that starburst events boost the  $X_{12/13}$  ratio.

## 5. MODELED CO-TO- $\text{H}_2$ CONVERSION FACTOR AT GMC SCALES

### 5.1. CO-to- $\text{H}_2$ conversion factor dependence on observables

#### 5.1.1. Dependence on CO $J=1-0$ intensity

Various simulations (e.g. Narayanan et al. 2012) have proposed that the bimodal distribution of  $\alpha_{\text{CO}}$  across

normal spiral galaxies and U/LIRGs can be accounted for by an  $\alpha_{\text{CO}}$  dependence on CO  $J=1-0$  intensity ( $I_{\text{CO } 1-0}$ ) at kpc scales. Recent simulations (e.g. Gong et al. 2020; Hu et al. 2022) have further pushed this dependence down to GMC spatial scales. However, it is hard to test this dependence at GMC scales in observations due to limited resolution and sensitivity of current instruments. Our study hence provides the first direct test of this dependence in starburst mergers. As shown in the left panel of Fig. 10, we see a significant anti-correlation between  $\alpha_{\text{CO}}$  and  $I_{\text{CO } 1-0}$ . Our fit power-law relation is

$$\log \alpha_{\text{CO}} = 0.77(\pm 0.04) - 0.3(\pm 0.02) \log I_{\text{CO}1-0} \quad (14)$$

The value in the bracket indicate the  $1-\sigma$  error for the fitted parameter.

Various simulations (e.g. Narayanan et al. 2012; Gong et al. 2020; Hu et al. 2022) predict the anti-correlation between  $\alpha_{\text{CO}}$  and the CO  $J=1-0$  integrated intensity. We overlay these simulation predictions in Fig. 10. We

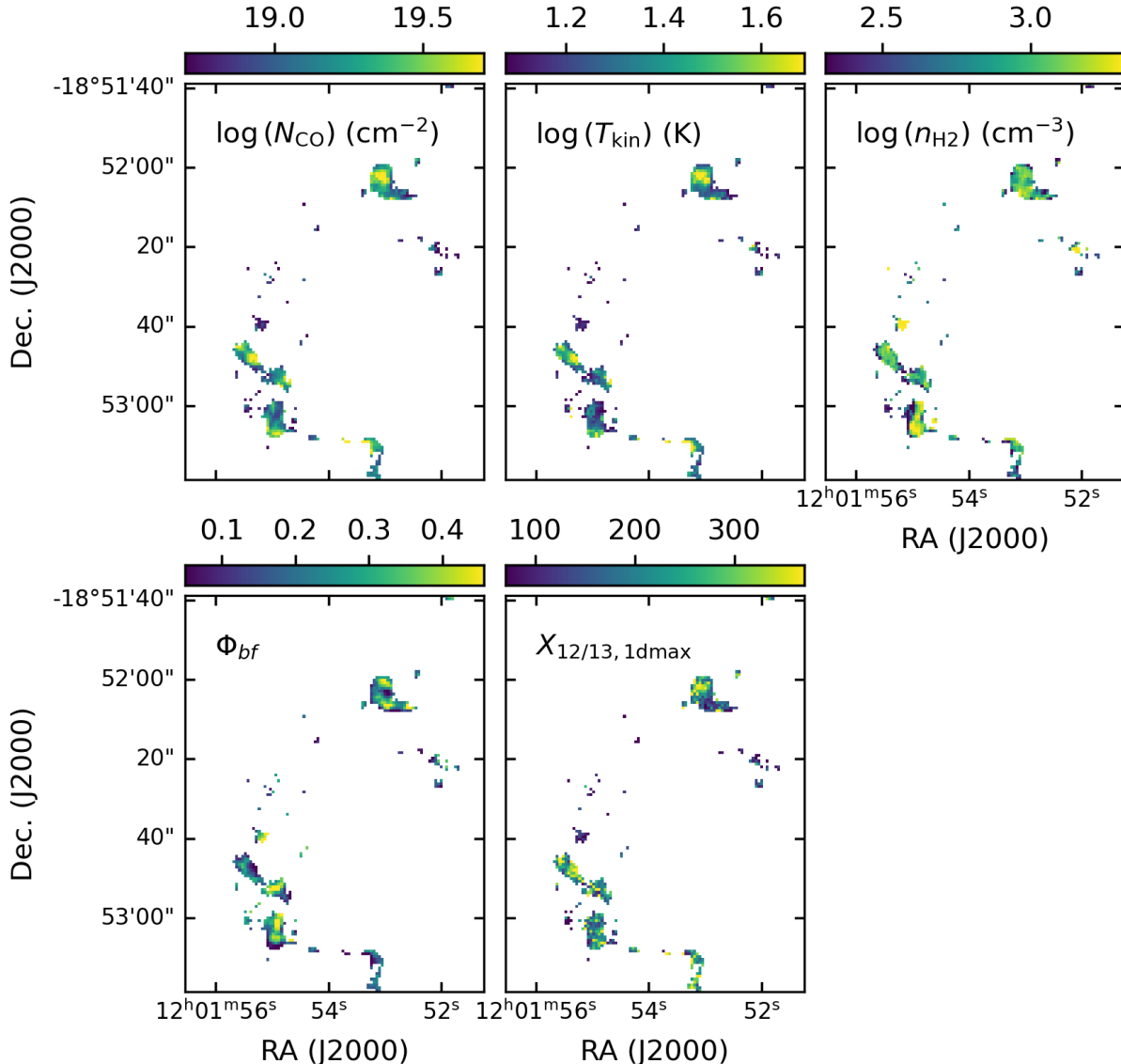


**Figure 8.** Maps of RADEX derived physical properties of the Antennae. The top row shows, from left to right, CO column density, kinetic temperature and molecular gas volume density. The bottom row shows the beam filling factor on the left and the  $[\text{CO}]/[^{13}\text{CO}]$  abundance ratio on the right. The maximal values for the color bars for all the quantities are set to be 95 percentile values.

can see that our power-law fit has almost the same slope as that predicted (slope of  $-0.32$ ) in Narayanan et al. (2012). On the other hand, the predictions from Gong et al. (2020) and Hu et al. (2022) give shallower slopes and tend to over-estimate  $\alpha_{\text{CO}}$  values. We note that both Gong et al. (2020) and Hu et al. (2022) have a simulation set-up with maximum  $I_{\text{CO } 1-0}$  barely reaching  $100 \text{ K km s}^{-1}$ . Therefore, it is possible that their predictions are more applicable to the environment in normal spiral galaxies with much lower gas surface densities. On the other hand, the simulation run in Narayanan et al. (2012) is more focused on the molecular gas in starburst

merger with similar environments as the Antennae. Despite similar slopes, the predicted  $\alpha_{\text{CO}}$  values based on the relation in Narayanan et al. (2012) is higher than our  $\alpha_{\text{CO}}$  measurement by a factor of 1.7. The offset in absolute values might be due to our arbitrary  $x_{\text{CO}}$  choice.

#### 5.1.2. Dependence on CO 1-0 optical depth and $^{13}\text{CO}/\text{CO}$ ratio

Recent GMC LVG modeling in normal spiral galaxies (Teng et al. 2022; Teng et al. 2023) suggests that  $\alpha_{\text{CO}}$  has a tight proportional correlation with the CO  $J=1-0$

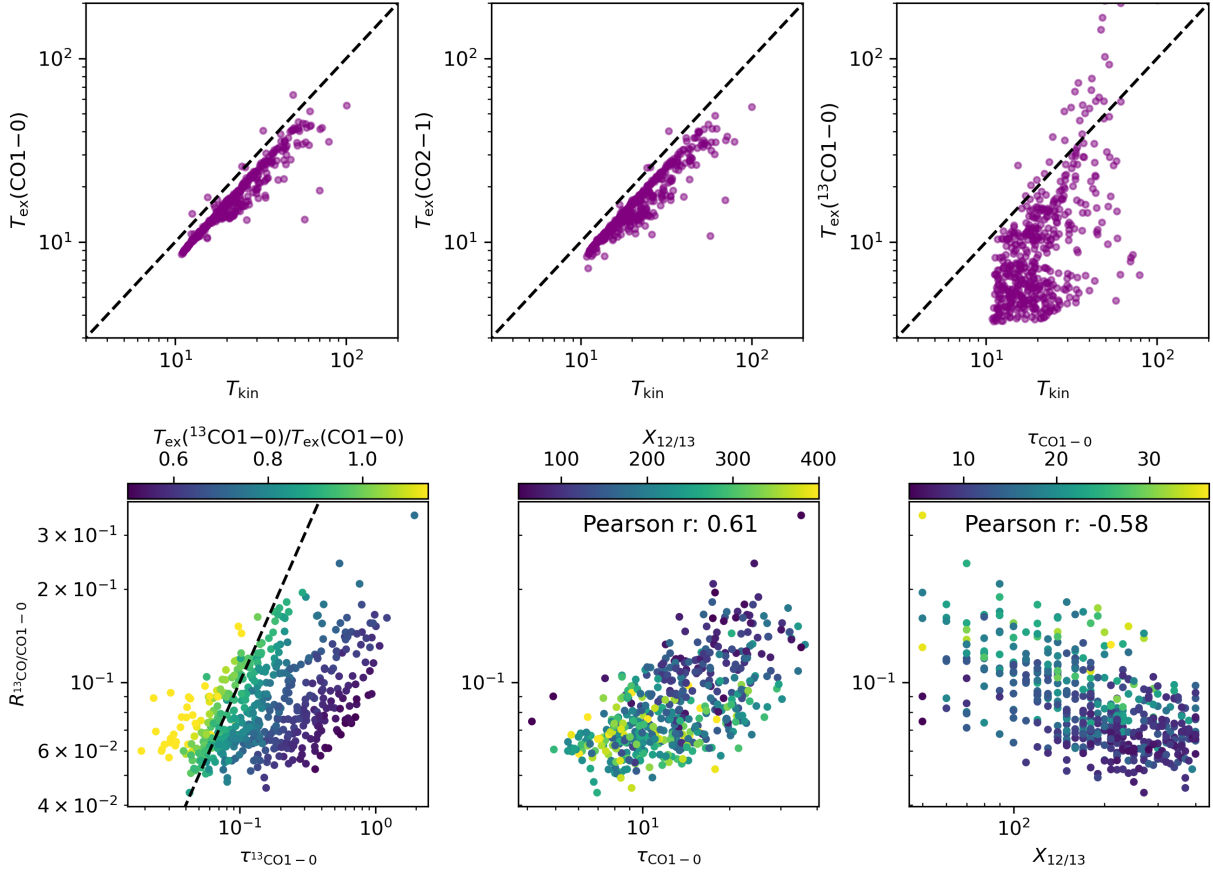


**Figure 9.** (*Upper*) The excitation temperature of CO  $J=1-0$ ,  $2-1$  and  $^{13}\text{CO } J=1-0$  versus the kinetic temperature. We can see both CO  $J=1-0$  and CO  $J=2-1$  emissions are thermally excited (The excitation temperature is slightly lower than the kinetic temperature probably because the kinetic temperature is only sampled down to 10K, which affects the PDF of  $T_{\text{kin}}$  and shift the median to slightly higher values). On the other hand, most  $^{13}\text{CO } J=1-0$  emission is subthermally excited. (*Lower left*) The  $R_{13\text{CO}/\text{CO}1-0}$  ratio versus  $^{13}\text{CO } J=1-0$  optical depth. We can see when  $^{13}\text{CO } J=1-0$  is thermally excited ( $T_{\text{ex}}(^{13}\text{CO}1-0)/T_{\text{ex}}(\text{CO}1-0) \approx 1$ ),  $R_{13\text{CO}/\text{CO}1-0}$  ratio is roughly equal to the  $^{13}\text{CO } J=1-0$  optical depth (dashed line), as expected under LTE conditions. (*Lower middle*)  $R_{13\text{CO}/\text{CO}1-0}$  versus  $\tau_{\text{CO}1-0}$  and (*lower right*)  $X_{12/13}$  abundance ratio. We can see  $R_{13\text{CO}/\text{CO}1-0}$  has strong correlation with both quantities.

optical depth ( $\tau_{\text{CO}1-0}$ ) when  $\tau_{\text{CO}(1-0)} > 1$ . This relation is consistent with our LVG modeling expectation. Under the LVG assumption, we have

$$\tau_{\text{CO}1-0} \propto N_{\text{CO}}/\Delta v \quad (15)$$

As shown in Section 4.1, most CO  $J=1-0$  emission is thermally excited with  $R_{\text{CO}2-1/1-0} \sim 1$ . Based on the LTE assumption, we have

$$\begin{aligned} T_{\text{peak}} &= \Phi_{\text{bf}} T_{\text{exc}} [1 - \exp(-\tau_{\text{CO}1-0})] \\ &\approx \Phi_{\text{bf}} T_{\text{kin}} [1 - \exp(-\tau_{\text{CO}1-0})] \end{aligned} \quad (16)$$

Substituting these two equations into Eq. 8, we have

$$\begin{aligned} \alpha_{\text{CO}} &= \frac{N_{\text{CO}} \Phi_{\text{bf}}}{x_{\text{co}} I_{\text{CO}(1-0)}} = \frac{N_{\text{CO}}/\Delta v}{x_{\text{co}} T_{\text{peak}}} \Phi_{\text{bf}} \\ &\propto \frac{\tau_{\text{CO}1-0}}{1 - \exp(-\tau_{\text{CO}1-0})}, \quad (x_{\text{CO}}, T_{\text{kin}} = \text{const}) \quad (17) \\ &\propto \tau_{\text{CO}1-0}, \quad (\tau_{\text{CO}1-0} \gg 1) \end{aligned}$$

In the left panel of Fig. 11, we can see a tight linear correlation between  $\alpha_{\text{CO}}$  and  $\tau_{\text{CO}1-0}$ , which is consistent with this theoretical expectation. The red solid line is the proportional fit to the relation, which is

$$\log \alpha_{\text{CO}} = \log \tau_{\text{CO}1-0} - 1.05(\pm 0.01) \quad (18)$$

In real observations,  $\tau_{\text{CO}1-0}$  is hard to measure and generally requires multi-CO transition radiative transfer modeling. Various studies (e.g. Jiménez-Donaire et al. 2017) have proposed to use the  $^{13}\text{CO}/\text{CO}$  line ratio ( $R_{13\text{CO}/\text{CO}}$ ) to trace the optical depth of optically thick CO  $J=1-0$  line. Based on Eq. 13, we would expect  $R_{13\text{CO}/\text{CO}1-0} \propto \tau_{\text{CO}1-0}$  if the  $X_{12/13}$  abundance ratio is fixed. This scenario is also supported by Teng et al. (2023), where they found a strong correlation between  $\alpha_{\text{CO}}$  and  $R_{13\text{CO}/\text{CO}}$  based on  $J=2-1$  lines across three barred galaxy centers. As shown in the right panel of Fig. 11, we can see a strong correlation between  $\alpha_{\text{CO}}$

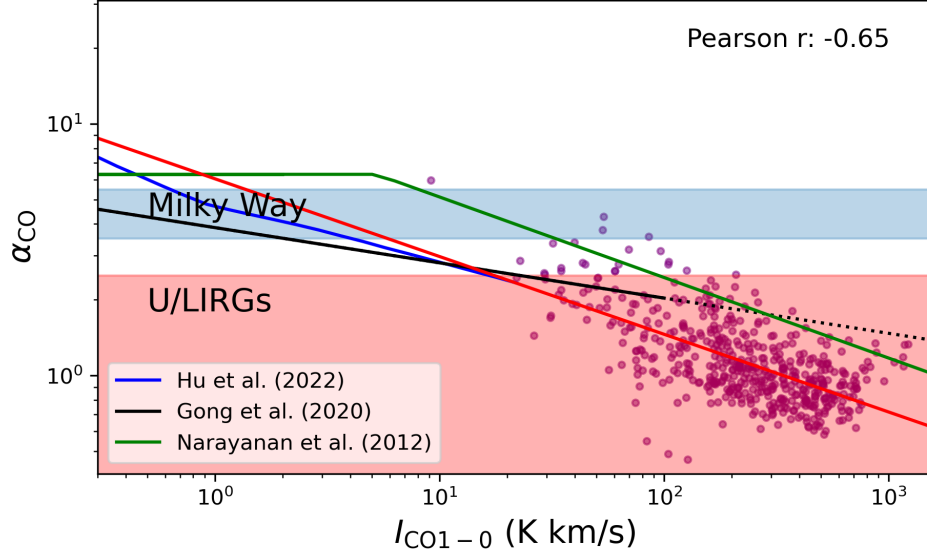


**Figure 10.** (*Left*) Modeled  $\alpha_{\text{CO}}$  versus CO  $J=1-0$  integrated intensity  $I_{\text{CO}(1-0)}$ . The red solid line is the fit to  $\alpha_{\text{CO}}$  versus  $I_{\text{CO}(1-0)}$  using data in this work. The solid line is the simulation prediction from Gong et al. (2020) at a resolution of 128 pc, the blue solid line is the simulation prediction from Hu et al. (2022) at a resolution of 125 pc and the green solid line is the simulation prediction from Narayanan et al. (2012). The dotted lines are extrapolated relations out of the corresponding simulation ranges. We can see a significant anti-correlation between  $\alpha_{\text{CO}}$  and  $I_{\text{CO}(1-0)}$  with a power-law slope closest to the prediction from Narayanan et al. (2012), which has the similar environmental set-up for starburst mergers such as the Antennae. The difference in power-law slope from other simulation predictions and observational fit might be due to the fact we are probing the environment with much higher gas surface density.

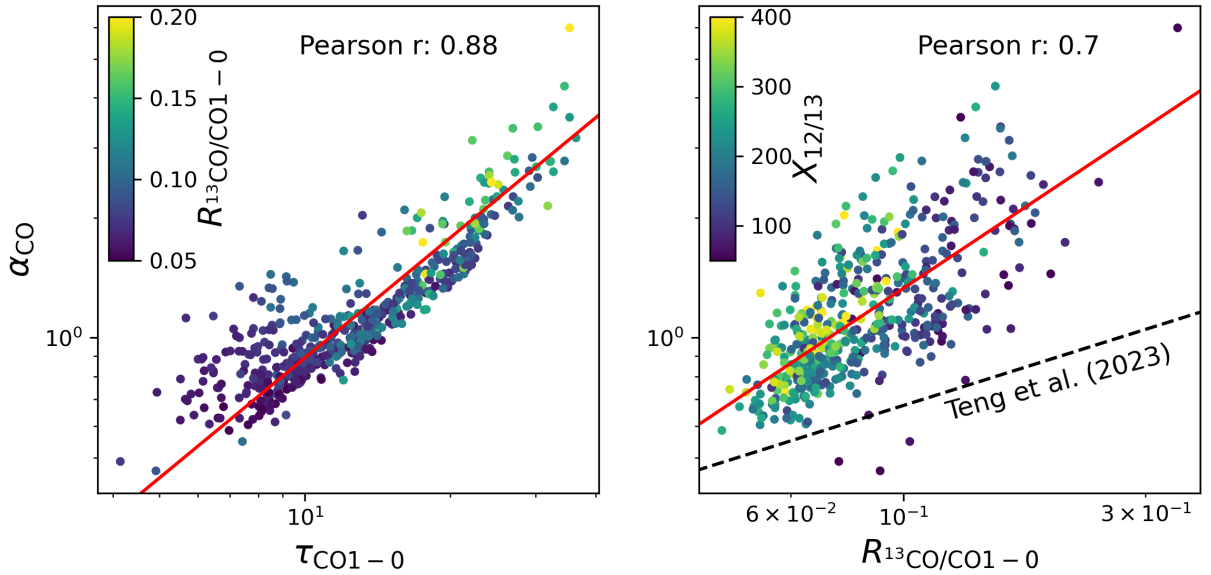


**Figure 11.** (*Left*) The modeled  $\alpha_{\text{CO}}$  versus the modeled  $\tau_{\text{CO}(1-0)}$  color coded by  $^{13}\text{CO}/\text{CO}$   $J=1-0$  ratio ( $R_{13\text{CO}/\text{CO}(1-0)}$ ). The red line is a proportional fit (power law slope of 1) to data points. (*Right*) Modeled  $\alpha_{\text{CO}}$  versus  $R_{13\text{CO}/\text{CO}(1-0)}$  color coded by  $[\text{CO}]/[^{13}\text{CO}]$  abundance ratio  $X_{12/13}$ . The red line is the power-law fit to the  $\alpha_{\text{CO}}$  versus  $R_{13\text{CO}/\text{CO}(1-0)}$  relation. The dashed line is the  $\alpha_{\text{CO}}$  versus  $R_{13\text{CO}/\text{CO}(2-1)}$  relation from Teng et al. (2023). We can see there is a tight linear correlation between  $\alpha_{\text{CO}}$  and  $\tau_{\text{CO}(1-0)}$  for the Antennae, which is consistent with results of Teng et al. (2022); Teng et al. (2023). We can also see a strong correlation between  $\alpha_{\text{CO}}$  and  $R_{13\text{CO}/\text{CO}(1-0)}$ , which suggests  $R_{13\text{CO}/\text{CO}(1-0)}$  can be potentially used as an  $\alpha_{\text{CO}}$  tracer.

and  $R_{13\text{CO}/\text{CO}_{1-0}}$ . We can still see a very strong correlation between  $\alpha_{\text{CO}}$  and  $R_{13\text{CO}/\text{CO}_{1-0}}$ , which suggests  $R_{13\text{CO}/\text{CO}_{1-0}}$  is a good indicator of  $\tau_{\text{CO}_{1-0}}$  and hence can be used to calibrate  $\alpha_{\text{CO}}$ . We fit the a power-law function between these two quantities and have

$$\log \alpha_{\text{CO}} = 0.85(\pm 0.04) \log R_{13\text{CO}/\text{CO}_{1-0}} + 0.97(\pm 0.04) \quad (19)$$

We can see that the  $\alpha_{\text{CO}}$  versus  $R_{13\text{CO}/\text{CO}_{1-0}}$  relation is still relatively close to linear as what we expect. We also overlay the  $\alpha_{\text{CO}}$  versus  $R_{13\text{CO}/\text{CO}_{2-1}}$  relation drawn from Teng et al. (2023). We can see their slope is shallower than us. It is partly due to our choice of different excitation lines. As shown in Appendix A,  $\alpha_{\text{CO}}$  versus  $R_{13\text{CO}/\text{CO}_{2-1}}$  for the Antennae also has a shallower slope than that versus  $R_{13\text{CO}/\text{CO}_{1-0}}$ . A possible explanation for the shallower slope of  $^{13}\text{CO}/\text{CO}$   $J=2-1$  ratio is that  $^{13}\text{CO}$   $J=2-1$  line might be more affected by the subthermal excitation effect and hence has weaker dependence on the optical depth variation. We also see offset between their and our absolute  $\alpha_{\text{CO}}$  values, which is also reflected in other  $\alpha_{\text{CO}}$  relations (e.g. see Section 5.1.3). As discussed in Section 5.2, our  $x_{\text{CO}}$  choice could affect the absolute  $\alpha_{\text{CO}}$  values.

We do see  $\alpha_{\text{CO}}$  versus  $R_{13\text{CO}/\text{CO}_{1-0}}$  relation has a significantly larger scatter compared to the  $\alpha_{\text{CO}}$  versus  $\tau_{\text{CO}_{1-0}}$  relation. As discussed in Section 4.2,  $R_{13\text{CO}/\text{CO}_{1-0}}$  is correlated with both  $\tau_{\text{CO}_{1-0}}$  and  $X_{12/13}$ . Therefore, the scatter in  $\alpha_{\text{CO}}$  versus  $R_{13\text{CO}/\text{CO}_{1-0}}$  can be caused by different  $X_{12/13}$  values in different regions. We therefore color code the  $\alpha_{\text{CO}}$  versus  $R_{13\text{CO}/\text{CO}_{1-0}}$  plot with  $X_{12/13}$  values (Fig. 11, right panel). As we can see, there is a clear trend that the larger  $\alpha_{\text{CO}}$  becomes, the higher  $X_{12/13}$  values the data points have. This confirms that the scatter in  $\alpha_{\text{CO}}$  versus  $R_{13\text{CO}/\text{CO}_{1-0}}$  relation mainly comes from  $X_{12/13}$  variation. We can incorporate  $X_{12/13}$  into our  $\alpha_{\text{CO}}$  versus  $R_{13\text{CO}/\text{CO}_{1-0}}$  relation to remove this systematic error. We perform the two variable fitting and get the updated relation as

$$\log \alpha_{\text{CO}} = 1.03(\pm 0.05) \log R_{13\text{CO}/\text{CO}_{1-0}} + 0.21(\pm 0.03) \log X_{12/13} + 0.7(\pm 0.06) \quad (20)$$

This function can be used to calibrate  $\alpha_{\text{CO}}$  values using  $^{13}\text{CO}/\text{CO}$  ratio given fiducial  $X_{12/13}$  values, which could potentially be applied to galactic environments rather than the Antennae.

### 5.1.3. Dependence on GMC velocity dispersion

As an optically thick line, CO  $J=1-0$  is often established as a molecular gas tracer based on the fact that the CO  $J=1-0$  luminosity is proportional to virial mass for individual GMCs in both the Milky Way and

nearby galaxies (references in Bolatto et al. 2013). However, GMCs in starburst systems might have larger velocity dispersion as perturbed by starburst/merging activities and hence less gravitationally bound. For a given fixed surface density, the increase in velocity dispersion could reduce the optical depth of the gas (Eq. 15) and hence reduce the  $\alpha_{\text{CO}}$  (Eq. 18). Early theoretical works (e.g. Downes et al. 1993) suggested that for starburst systems, CO instead trace the geometric mean of molecular gas mass and virial mass (i.e.  $L_{\text{CO}} \propto T_{\text{B},0} (M_{\text{gas}} M_{\text{vir}} / \rho_{\text{gas}})^{1/2}$ , see discussions in Shetty et al. 2011). However, it was hard to test these scaling relations due to the limited resolution of instruments at that time which made it hard to resolve individual GMCs. Papadopoulos et al. (2012) infer the dynamical states of GMCs in starburst U/LIRGs based on the LVG modeled volume density and velocity gradient and their results support the argument that  $\alpha_{\text{CO}}$  is lower in starburst systems due to GMCs being perturbed by the merging/starburst activities and hence out of virial equilibrium. However, with this indirect method, it is hard to capture the  $\alpha_{\text{CO}}$  variation within individual galaxies. Recent high-resolution ALMA observations (Teng et al. 2023; Teng et al. 2024) suggest a strong anti-correlation between  $\alpha_{\text{CO}}$  and GMC velocity dispersion in the center of spiral galaxies. However, this anti-correlation is yet to be tested in typical starburst galaxy mergers.

In Fig. 12, we see a significant anti-correlation between  $\alpha_{\text{CO}}$  and  $\sigma_v$ , which is consistent with our modeling expectation. We also fit the anti-correlation with a power-law function, which is

$$\log \alpha_{\text{CO}} = 0.7(\pm 0.04) - 0.46(\pm 0.03) \log \sigma_v \quad (21)$$

We also fit the  $\alpha_{\text{CO}}$  versus  $\sigma_v$  relation with a power law function with a fixed slope of -0.5, as labeled in red dashed line. This power-law slope is derived from theoretical prediction under the LVG approximation for two-level optically thick systems (see detailed discussion in Teng et al. (2024) and references therein). Under this approximation, the excitation temperature can be expressed as

$$T_{\text{ex}} \propto n_{\text{H}_2} \sqrt{\frac{R_{\text{GMC}} x_{\text{CO}}}{\sigma_v}} \quad (22)$$



where  $R_{\text{GMC}}$  is GMC radius. We can then substitute  $T_{\text{ex}}$  into Eq. 18 and get

$$\begin{aligned} \alpha_{\text{CO}} &= \frac{N_{\text{CO}}/\Delta v}{x_{\text{CO}}T_{\text{peak}}}\Phi_{\text{bf}} \\ &\propto \frac{N_{\text{CO}}/\sigma_v}{T_{\text{ex}}x_{\text{CO}}}, \quad (T_{\text{ex}} \approx T_{\text{peak}}/\Phi_{\text{bf}}, \text{ optically thick}) \\ &\propto \sqrt{\frac{R_{\text{GMC}}}{x_{\text{CO}}\sigma_v}} \\ &\propto \sigma_v^{-0.5} \end{aligned} \quad (23)$$

We can see that our fit power-law function is hence quite close to the theoretical prediction, which suggests that the variation in velocity dispersion could be the major driver to the  $\alpha_{\text{CO}}$  variation. Furthermore, this suggests that we can use velocity dispersion to calibrate the  $\alpha_{\text{CO}}$  variation at GMC scales.

We also overplot the  $\alpha_{\text{CO}}$  versus  $\sigma_v$  fit from Teng et al. (2023); Teng et al. (2024). We can see our data align relatively well with the calibrated relation in Teng et al. (2024) using dust-based approach (Sandstrom et al. 2013b). However, our  $\alpha_{\text{CO}}$  values are significantly higher than the calibrated relation in Teng et al. (2023). Teng et al. (2024) suggest that the discrepancy between their calibrated  $\alpha_{\text{CO}}$  versus  $\sigma_v$  relation using the two methods might be due to their overestimate of  $x_{\text{CO}}$  adopted in the LVG modeling. As discussed in Section 5.2, our adopted value of  $x_{\text{CO}} = 3 \times 10^{-4}$  is reasonable. However, Teng et al. (2023) studies molecular gas in the center of normal spiral galaxies, which might have lower  $x_{\text{CO}}$  values than in our starburst galaxy mergers.

#### 5.1.4. Dependence on CO line ratios

It has been proposed recently by Gong et al. (2020) that the CO  $J=2-1/1-0$  ratio  $R_{\text{CO}2-1/1-0}$  can be used as a tracer of  $\alpha_{\text{CO}}$ . For individual GMCs in virial equilibrium, we would expect the relation (Gong et al. 2020)

$$\alpha_{\text{CO}} \propto \begin{cases} T_{\text{exc}}^{-1/2}, & \text{low density} \\ \frac{\sqrt{n}}{T_{\text{kin}}}, & \text{high density,} \end{cases} \quad (24)$$

where  $T_{\text{exc}}$  is the CO  $J=1-0$  excitation temperature,  $T_{\text{kin}}$  is the gas kinetic temperature and  $n$  is the gas volume density. In the low volume density regime, we have an anti-correlation between  $\alpha_{\text{CO}}$  and  $T_{\text{exc}}$ . Since higher  $T_{\text{exc}}$  will directly lead higher  $R_{\text{CO}2-1/1-0}$  ratio, we would expect an anti-correlation between  $\alpha_{\text{CO}}$  and  $R_{\text{CO}2-1/1-0}$ . In Fig. A1, we see no correlation between these two quantities, which is probably due to our limited range of  $R_{\text{CO}2-1/1-0}$  values (Fig. 6). Furthermore, as discussed in Section 4.1, the  $R_{\text{CO}2-1/1-0}$  ratio

of GMCs in the Antennae is close to 1, which suggests they are in LTE condition with high gas volume density. In this case, we no longer expect an anti-correlation between  $\alpha_{\text{CO}}$  and  $R_{\text{CO}2-1/1-0}$ .

Since  $R_{\text{CO}2-1/1-0}$  saturates to  $\sim 1$ , it is likely the CO excitation condition is traced by ratios between higher- $J$  CO lines, such as CO  $J=3-2$ , and CO  $J=1-0$ . We therefore also test how  $\alpha_{\text{CO}}$  correlates with  $R_{\text{CO}3-2/1-0}$ . As we can see,  $R_{\text{CO}3-2/1-0}$  shows a significantly larger range of values than  $R_{\text{CO}2-1/1-0}$ . However, we can only see a very weak anti-correlation between  $\alpha_{\text{CO}}$  and  $R_{\text{CO}3-2/1-0}$ . The weak correlation between  $\alpha_{\text{CO}}$  and CO line ratios suggest that excitation condition does not play a major role in  $\alpha_{\text{CO}}$  variation within starburst mergers. This is consistent with the observational studies in Teng et al. (2023) for the center of spiral galaxies, where they find temperature only has minor ( $\sim 20\%$ ) contribution to  $\alpha_{\text{CO}}$  variations. Simulations, such as Bournaud et al. (2015), also find that  $\alpha_{\text{CO}}$  has weak or no correlation with high- $J$  CO to CO  $J=1-0$  line ratios in starburst mergers. Bournaud et al. (2015) also find that the major cause of low  $\alpha_{\text{CO}}$  in starburst mergers is higher velocity dispersion instead of higher gas temperature in these systems compared to other types of galaxies.

We can also see from Fig. A1 that our modeled  $\alpha_{\text{CO}}$  is mostly below the simulation prediction from Gong et al. (2020). This could be due to other environmental factors, such as higher CO intensities that contributes to lower the  $\alpha_{\text{CO}}$  values in the Antennae.

#### 5.1.5. Summary

The  $\alpha_{\text{CO}}$  map is shown in Fig. 14. As we show in previous sections,  $\alpha_{\text{CO}}$  is tightly correlated with CO  $J=1-0$  optical depth ( $\tau_{\text{CO}1-0}$ ) so the two maps look quite similar.  $\alpha_{\text{CO}}$  also has relatively strong anti-correlation with CO  $J=1-0$  integrated intensity ( $I_{\text{CO}1-0}$ ) and velocity dispersion ( $\sigma_v$ ). We can also see that the low  $\alpha_{\text{CO}}$  regions generally coincides with the high  $\Sigma_{\text{mol}}$  regions, which also has relatively low optical depth. For these regions, the low optical depth is most likely to be caused by the increase in velocity dispersion, which allows more CO  $J=1-0$  emission to be transmitted out.

#### 5.2. Constrain $x_{\text{CO}}$ abundance ratio with dust continuum

From the dust continuum map, we can then calculate the dust mass as (Wilson et al. 2008)

$$M_{\text{dust}} = 74220 S_{880} D^2 \frac{\exp(17/T_{\text{dust}})}{\kappa} \quad (25)$$

where  $S_{880}$  is the flux in Jy,  $D$  is the distance in Mpc,  $T_{\text{dust}}$  is the dust temperature in Kelvin and  $\kappa$  is the dust

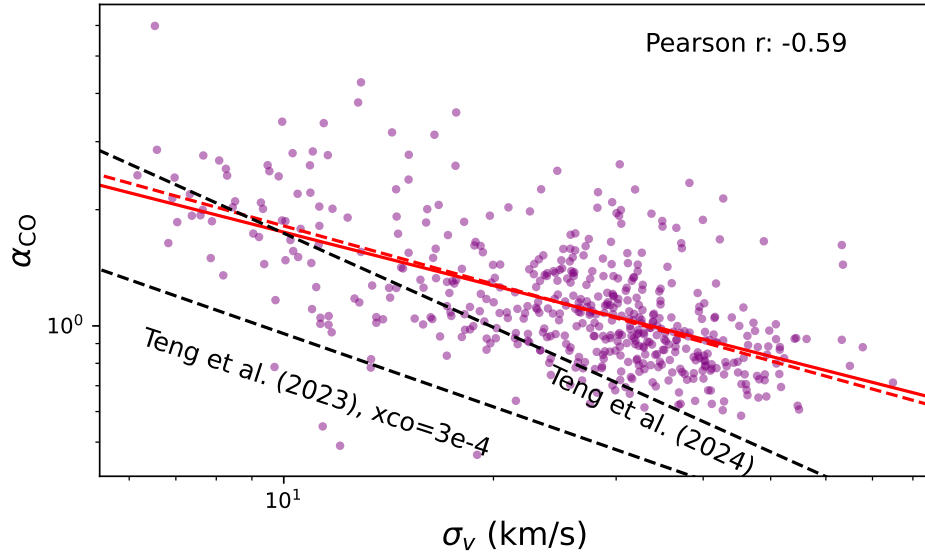


**Figure 12.**  $\alpha_{\text{CO}}$  versus velocity dispersion  $\sigma_v$ . The red solid line is the power-law fit of the relation and the red dashed line is the power-law fit with fixed slope of -0.5 from theoretical predictions (see Section 5.1.3 for detailed discussion). The two dashed lines indicate the relation found in Teng et al. (2023); Teng et al. (2024). We can see a strong anti-correlation between  $\alpha_{\text{CO}}$  and  $\sigma_v$  consistent with theoretical prediction, which suggests that the increase in velocity dispersion is responsible for bringing down  $\alpha_{\text{CO}}$  in starburst galaxy mergers.

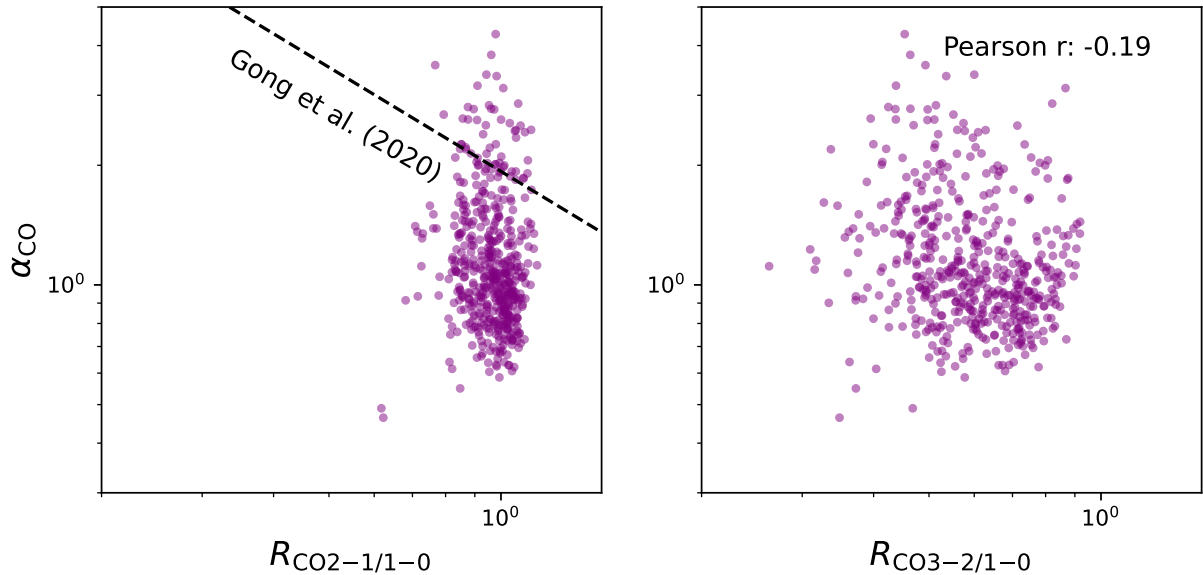


**Figure 13.**  $\alpha_{\text{CO}}$  versus CO  $J=2-1/1-0$  ratio  $R_{\text{CO}2-1/1-0}$  (left) and CO  $J=3-2/1-0$  ratio  $R_{\text{CO}3-2/1-0}$  (right). The dashed line is the simulation fitting results from Gong et al. (2020). We can see there is no correlation between  $\alpha_{\text{CO}}$  and  $R_{\text{CO}2-1/1-0}$  due to CO  $J=2-1$  being thermalized, which saturates the ratio at values close to 1. We also do not see a significant anti-correlation between  $\alpha_{\text{CO}}$  and  $R_{\text{CO}3-2/1-0}$ , which suggests that CO line ratios are generally not a good tracer of  $\alpha_{\text{CO}}$  variation in starburst systems with large gas surface densities.

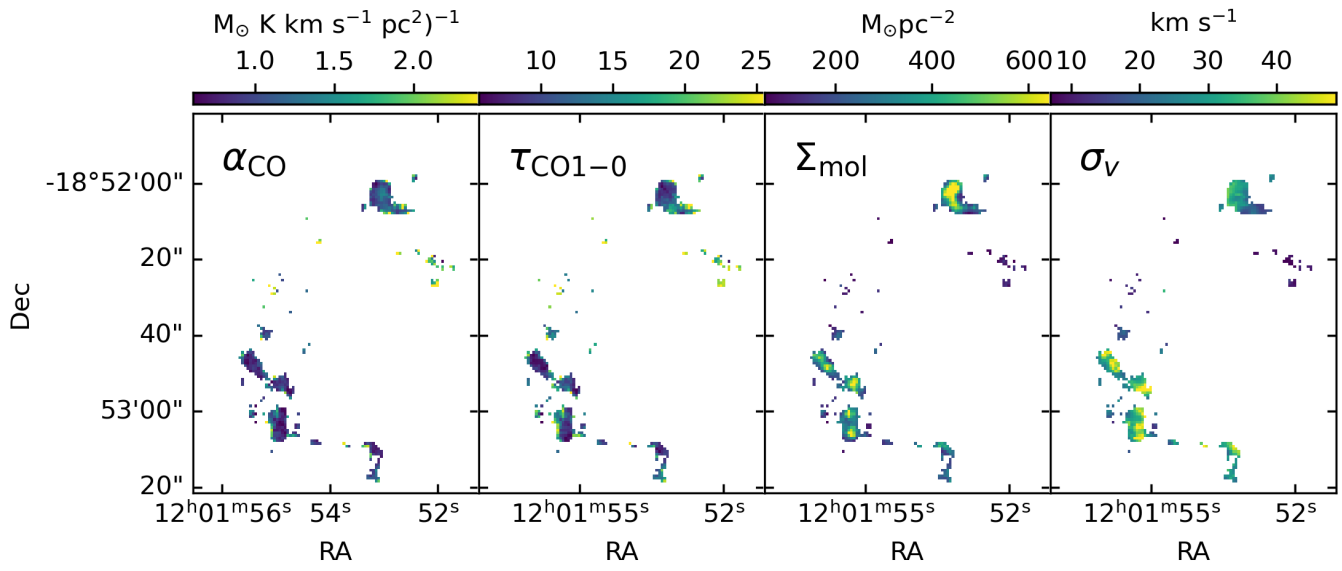


Figure 14. The derived maps of  $\alpha_{\text{CO}}$ ,  $\tau_{\text{CO1-0}}$ ,  $\Sigma_{\text{mol}}$  and  $\sigma_v$  for the Antennae.

opacity in  $\text{g}^{-1} \text{cm}^2$ . We chose  $0.9 \text{ g}^{-1} \text{cm}^2$  as the fiducial value for  $\kappa$  (Wilson et al. 2008) but note that  $\kappa$  can be a factor of 2 higher in starburst systems (Wilson et al. 2014). The dust surface density for a given pixel can then be calculated as

$$\begin{aligned} \Sigma_{\text{dust}} &= M_{\text{dust}} / (1.1331 B_{\text{FWHM}}^2) \\ &= 2.9 I_{880} D^2 \frac{\exp(17/T_{\text{dust}})}{\kappa} \left( \frac{B_{\text{FWHM}}}{150 \text{ pc}} \right)^{-2} \quad (26) \end{aligned}$$

where  $I_{880}$  is the intensity in Jy/beam and  $B_{\text{FWHM}}$  is the FWHM of the round beam in pc. One of the major uncertainties in the dust mass calculation comes from the unconstrained dust temperature. We adopt the dust temperature from Klaas et al. (2010) for pixels in each defined subregion (Fig. 3). For subregion A1a which does not have a temperature measurement, we assume the temperature to be the same as the overall dust temperature derived from the integrated fluxes of the entire galaxy.

The comparison of  $\Sigma_{\text{mol}}$  and  $\Sigma_{\text{dust}}$  is shown in the left panel of Fig. 15. We can see that a high  $x_{\text{CO}}$  value is favored in order to get a reasonable gas-to-dust ratio (GDR) below 200. Furthermore, since our modeling is targeting the most dense GMCs, we would expect them to have GDR values closer to dense gas values of 50 – 100 instead of most diffuse medium values of 200 (Remy et al. 2017). Instead, if we assume a constant Milky Way  $\alpha_{\text{CO}}$  value, we will get GDR values of 300 – 400 (consistent with GDR values in Klaas et al. 2010, adopting the Milky Way  $\alpha_{\text{CO}}$ ).

An alternative explanation is that the Antennae might actually have a high GDR values. However, Gunawardhana et al. (2020) derive the metallicity map for the Antennae and find most of regions in the Antennae have solar metallicity. Therefore, we would not expect the Antennae to have abnormally high GDR values.

We note that the dust mass we calculate is also affected by systematic uncertainties from other free parameters, such as dust temperature ( $T_{\text{dust}}$ ) and opacity ( $\kappa$ ). The right two panels in Fig. 15 show how changing  $x_{\text{CO}}$ ,  $T_{\text{dust}}$  and  $\kappa$  can affect our calculated GDR value. If we adopt a standard  $\kappa$  value of  $0.9 \text{ g}^{-1} \text{cm}^2$ , we need both high  $x_{\text{CO}}$  values ( $> 2.5 \times 10^{-4}$ ) and low dust temperature ( $\sim 20 \text{ K}$ ) to keep the GDR value around 100. If we adopt a typical  $\kappa$  value for starburst galaxies ( $\sim 1.9 \text{ g}^{-1} \text{cm}^2$ ), we even need higher  $x_{\text{CO}}$  values to keep the GDR around the same value. The upper limit of  $x_{\text{CO}}$  of  $3 \times 10^{-4}$  is set by the measured  $[\text{C}]/[\text{H}]$  abundance ratio of  $1.5 \times 10^{-4}$  in the Milky Way (Sofia et al. 2004). Overall, we find it requires  $x_{\text{CO}}$  of  $\sim 3 \times 10^{-4}$  to give us a reasonable GDR value. This is also consistent with simulation predictions (e.g. Hu et al. 2022), which

shows that  $x_{\text{CO}}$  saturates at its maximal when the CO column density is greater than  $10^{18} \text{ cm}^{-2}$ . Based on our modeling results, most pixels have CO column density greater than that value.

### 5.3. GMC dynamical states in the Antennae

As discussed in He et al. (2023), the variation of  $\alpha_{\text{CO}}$  can lead to an uncertainty of a factor of 4 for GMC virial parameter ( $\alpha_{\text{vir}}$ ) measurements, hence affecting our judgement on GMC dynamical states in galaxy mergers. With our modeled  $\alpha_{\text{CO}}$ , we can put a more accurate constraint on GMC dynamical states in the Antennae. Although the absolute values of our modeled  $\alpha_{\text{CO}}$  depend on our  $x_{\text{CO}}$  choice, we have found in Section 5.2 that  $x_{\text{CO}} = 3 \times 10^{-4}$  is a reasonable assumption to give us realistic GDR values. With  $x_{\text{CO}} = 3 \times 10^{-4}$ , most of our modeled  $\alpha_{\text{CO}}$  are closer to U/LIRG values of  $1.1 M_{\odot} (\text{K km s}^{-1} \text{pc}^2)^{-1}$ , which is different from previous works that suggest that the Antennae should have a Milky Way  $\alpha_{\text{CO}}$  of  $4.3 M_{\odot} (\text{K km s}^{-1} \text{pc}^2)^{-1}$  (e.g. Zhu et al. 2003; Schirm et al. 2014). This conclusion in general will bring up the  $\alpha_{\text{vir}}$  of the Antennae, which suggests GMCs in the Antennae are less gravitationally bound than we might expect. As shown Fig. 16, our modeled  $\alpha_{\text{CO}}$  results suggest GMCs in the Antennae are more turbulent, which is consistent with the simulation prediction from He et al. (2023).

We can also see that in spite of occupying a different parameter space, our modeled  $\alpha_{\text{CO}}$  gives a similar contour shape as adopting a constant Milky Way  $\alpha_{\text{CO}}$  (Fig. 16). This similarity suggests that the absolute value of global  $\alpha_{\text{CO}}$  matters more than the relative  $\alpha_{\text{CO}}$  variation within the galaxy in determining the overall GMC dynamical states in the Antennae. We note that most past literature studies suggest a Milky Way  $\alpha_{\text{CO}}$  in the Antennae. Wilson et al. (2003) first suggested this value based on comparison between virial mass and CO  $J=1-0$  luminosity. However, as we have discussed above, GMCs in starburst systems are not necessarily in virial equilibrium. Schirm et al. (2014) also suggest a typical  $\alpha_{\text{CO}}$  value of  $\sim 7 M_{\odot} (\text{K km s}^{-1} \text{pc}^2)^{-1}$  based on two-component LVG modeling assuming  $x_{\text{CO}} = 3 \times 10^{-5}$ . They choose this value so that the hot component of gas from CO LVG modeling is comparable to the mass derived from  $\text{H}_2$  emission. However, Harrington et al. (2021) suggest that the high- $J$  CO transition fluxes that are used to constrain the second component might come from cold dense gas instead of hot diffuse gas, and hence not necessarily trace the same gas component as  $\text{H}_2$  emission. If we adopt our preferred  $x_{\text{CO}}$  value of  $3 \times 10^{-4}$ , the  $\alpha_{\text{CO}}$  derived from Schirm et al. (2014) is consistent with our results.

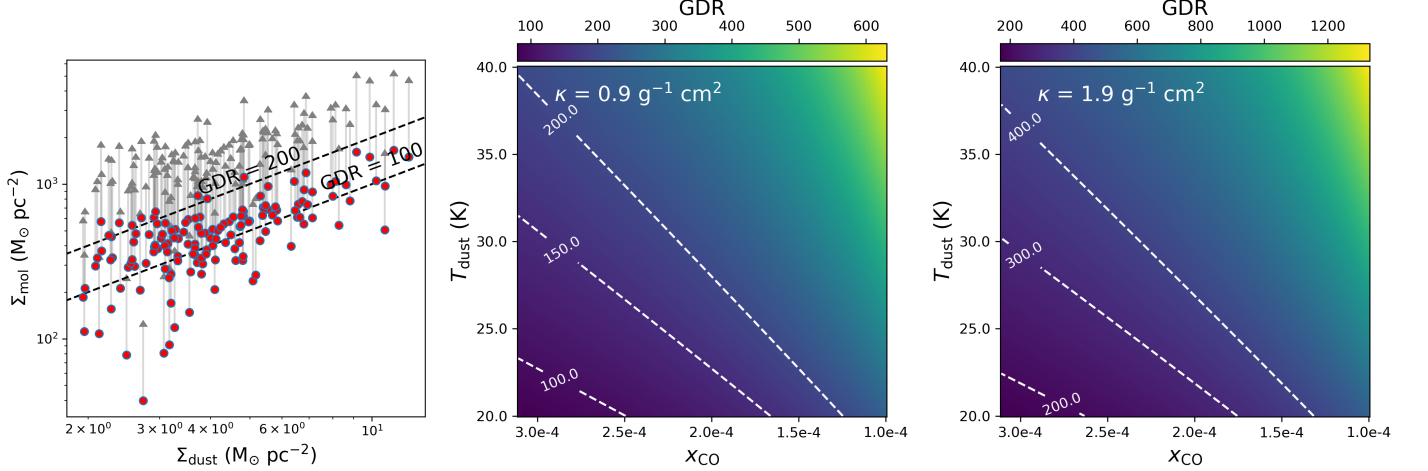


**Figure 15.** (Left) Molecular gas versus dust surface density.  $\Sigma_{\text{mol}}$  is calculated using our modeled  $\alpha_{\text{CO}}$  values. Red circles and gray arrows indicate  $\Sigma_{\text{mol}}$  calculated assuming  $x_{\text{CO}} = 3\text{e-}4$  and  $1\text{e-}4$  respectively. The dashed lines indicate constant gas-to-dust ratio (GDR). We can see that  $x_{\text{CO}} = 3 \times 10^{-4}$  gives us more realistic GDR values. (Middle) Median GDR distribution in the  $T_{\text{dust}}$  vs  $x_{\text{CO}}$  plane assuming  $\kappa = 0.9 \text{ g}^{-1} \text{ cm}^2$ . The dashed line indicate constant GDR values. (Right) Same as middle panel but assuming  $\kappa = 1.9 \text{ g}^{-1} \text{ cm}^2$ . We can see that a high  $x_{\text{CO}}$  value is favored in order to get a GDR below 200.

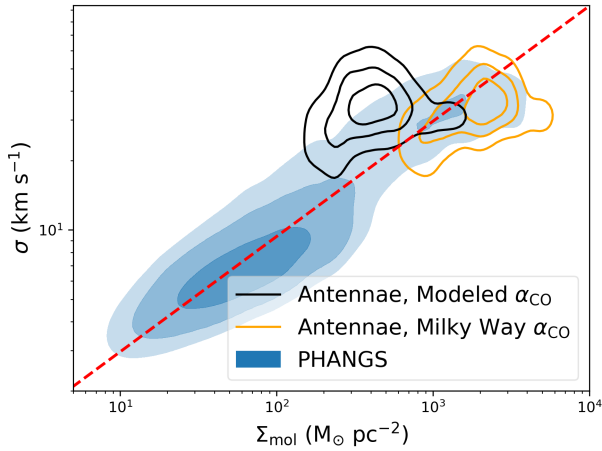


**Figure 16.** Velocity dispersion versus gas surface density contours for PHANGS galaxies (blue shaded) and the Antennae using varying  $\alpha_{\text{CO}}$  from this work (black) and a constant Milky Way  $\alpha_{\text{CO}}$  value (orange). The red dashed line marks the position of the median value of  $\alpha_{\text{vir}}$  for PHANGS galaxies of 2.7 (Sun et al. 2020a). Our modeled  $\alpha_{\text{CO}}$  results suggest that GMCs in the Antennae are less gravitationally bound than GMCs in the PHANGS galaxies.

## 6. MODELED CO-TO-H<sub>2</sub> CONVERSION FACTOR AT KPC SCALES

### 6.1. Modeling setup

We generally follow the same procedure as in Section 3.1 and 3.2 in modeling  $\alpha_{\text{CO}}$  at kpc scales. The difference in generating the modeling grids is that we sample the beam filling factor in log space ( $\log \Phi_{\text{bf}}$  from -3 to 0 with step of 0.1). This is because we expect the beam filling factor at kpc scales could be

much lower than 0.1. For the  $\alpha_{\text{CO}}$  modeling results, we apply a similar selection procedure to exclude pixels with one or more modeled quantities at the edge of our parameter space. Specifically, we exclude the pixels with  $X_{12/13,1\text{dmax}} \leq 30$ ,  $\log T_{\text{kin},1\text{dmax}} < 1.1$  or  $\log T_{\text{kin},1\text{dmax}} > 2$ .

### 6.2. $\alpha_{\text{CO}}$ comparison at GMC and kpc scales

Most previous studies on constraining the  $\alpha_{\text{CO}}$  have been done at kpc scales (e.g. Papadopoulos et al. 2012). Previous simulations (e.g. Narayanan et al. 2012) argue that  $\alpha_{\text{CO}}$  should be a scale-free parameter down to cloud scale. However, there has been no observational evidence to test this statement yet due to limited resolution and sensitivity. In the Antennae, we have enough resolution elements and detections at both kpc and GMC scales to be able to perform this comparison.

We generate the  $\alpha_{\text{CO}}$  map at kpc scale by applying the same procedure as in Section 3 using the combo masked CO moment maps at 1 kpc resolution generated from the PHANGS-ALMA pipeline. To match the  $\alpha_{\text{CO}}$  maps at 150 pc and 1 kpc resolution, we regrid the 150 pc map to have the same pixel size as that of the 1 kpc map. For each regridded 150 pc map pixel,  $\alpha_{\text{CO}}$  is calculated as the CO  $J=1-0$  intensity averaged value of the smaller pixels that are associated with the regridded pixel,

$$\langle \alpha_{\text{CO},150\text{pc}} \rangle_{1\text{kpc}} = \frac{\sum \alpha_{\text{CO},150\text{pc}} I_{\text{CO}(1-0)}}{\sum I_{\text{CO}(1-0)}} \quad (27)$$

The comparison between  $\alpha_{\text{CO}}$  at both scales is shown in the upper panels of Fig. 17. We can see that  $\alpha_{\text{CO}}$  values at kpc scale is about 60% of the CO  $J=1-0$  intensity averaged  $\alpha_{\text{CO}}$  values at 150 pc scale. It is possible

that kpc-scale CO emission includes diffuse component that is not detected at GMC scales. This diffuse component is warmer and more luminous and hence would have lower  $\alpha_{\text{CO}}$  values (Schirm et al. 2014; Kamenetzky et al. 2017). To quantify this effect, we calculate the fraction of the emission at kpc scale that comes from dense GMCs. For each kpc-scale pixel, the total flux of GMC emission is calculated by summing up fluxes of all pixels in the 150 pc resolution map associated with the kpc-scale pixel and with valid  $\alpha_{\text{CO}}$  values. Then the fraction is calculated as

$$f_{\text{GMC}} = \frac{\sum F_{\text{CO}(1-0)}^{150\text{pc}}}{F_{\text{CO}(1-0)}^{1\text{kpc}}} \quad (28)$$

where  $F_{\text{CO}(1-0)}^{150\text{pc}}$  and  $F_{\text{CO}(1-0)}^{1\text{kpc}}$  are the CO  $J=1-0$  flux of each pixel at GMC scale and kpc scale respectively. In the upper left panel of Fig. 17, we color code the data points with  $f_{\text{GMC}}$ . As shown in the upper left panel of Fig. 17, data points with high fraction ( $\sim 100\%$ ) are closer to the 1-to-1 line, which is consistent with our expectation. We also split the data into two categories with  $f_{\text{GMC}}$  greater or smaller than 50% (Fig. 17, upper middle and right panel). As we can see, for pixels with  $f_{\text{GMC}} > 50\%$ , kpc-scale  $\alpha_{\text{CO}}$  are  $\sim 70\%$  of the GMC  $\alpha_{\text{CO}}$  while for  $f_{\text{GMC}} < 50\%$ , the average kpc-scale  $\alpha_{\text{CO}}$  is  $\sim 43\%$  of GMC  $\alpha_{\text{CO}}$ . We also calculate the Pearson correlation coefficient between  $\alpha_{\text{CO},1\text{kpc}}/\langle\alpha_{\text{CO},150\text{pc}}\rangle_{1\text{kpc}}$  and  $f_{\text{GMC}}$  and find a strong correlation between these two quantities with the coefficient of 0.62.

However, it is still under debate whether the diffuse component of molecular gas has higher or lower  $\alpha_{\text{CO}}$  compared to cold dense gas in GMCs. Liszt, Pety & Lucas (2010) show that  $\alpha_{\text{CO}}$  is relatively constant among different molecular gas components in our Milky Way. They suggest this constant  $\alpha_{\text{CO}}$  should be attributed to the offsetting effects of lower CO abundances with respect to  $\text{H}_2$  ( $x_{\text{CO}}$ ) and a large  $I_{\text{CO}}/N_{\text{CO}}$  ratio in low extinction gas. Recent studies by Ramambason et al. (2023) further suggest that the abundance factor plays a more dominant role and hence actually increases  $\alpha_{\text{CO}}$  in diffuse molecular gas. We note that our modeling does not have the ability to constrain  $x_{\text{CO}}$ . Therefore, the  $\alpha_{\text{CO}}$  we modeled is proportional to the  $N_{\text{CO}}/I_{\text{CO}}$  ratio and hence does not reflect any  $\alpha_{\text{CO}}$  change due to CO abundance variation. For example, if the diffuse gas actually has lower  $x_{\text{CO}}$ , we would expect the actual  $\alpha_{\text{CO}}$  at kpc scale to be higher than our modeled values.

### 6.3. $\alpha_{\text{CO}}$ dependence at kpc scale

Due to limited resolution and sensitivity, previous studies are mostly focused on the kpc-scale  $\alpha_{\text{CO}}$  calibrations (e.g. Narayanan et al. 2012; Bolatto et al.

2013). These  $\alpha_{\text{CO}}$  prescriptions are widely applied to nearby galaxies (e.g. Sun et al. 2023). While these prescriptions generally catch the galaxy-to-galaxy variation, they are less well tested for  $\alpha_{\text{CO}}$  variation within individual galaxies, specifically for distant starburst galaxies that are hard to get resolved observations. Our observations of the Antennae provide an ideal test ground for kpc-scale  $\alpha_{\text{CO}}$  variation within galaxies, specifically starburst systems. Besides metallicity dependence,  $\alpha_{\text{CO}}$  is also found to be dependent on CO  $J=1-0$  intensity (Narayanan et al. 2012) and total (stellar+gas) surface density (Bolatto et al. 2013). Therefore, we test these two dependencies in the Antennae (Fig. 18).

In the left panel of Fig. 18, we show  $\alpha_{\text{CO}}$  versus  $I_{\text{CO}1-0}$  in comparison with simulation predictions. We can see a negative correlation between these two quantities with slope (-0.3) close to the two simulation predictions (-0.32 for Narayanan et al. 2012, -0.43 for Hu et al. 2022). We also see offsets between observed and simulation predicted absolute values. We note that the simulation by Hu et al. (2022) is focused on a typical kpc-size disk region in the Milky Way with a maximum  $I_{\text{CO}1-0}$  of 1 K km s<sup>-1</sup> at kpc scales. Our observed  $I_{\text{CO}1-0}$  is clearly out of this range. We also note that our  $\alpha_{\text{CO}}$  versus  $I_{\text{CO}1-0}$  correlation at GMC scale is in relatively good agreement with Hu et al. (2022) prediction (Fig. 10). Therefore, the discrepancy in the kpc-scale  $\alpha_{\text{CO}}$  versus  $I_{\text{CO}1-0}$  correlation might be caused by difference in GMC beam filling factor at kpc scales. If the number of GMCs inside the simulated kpc box were increased, we would expect higher kpc-scale  $I_{\text{CO}1-0}$  for a given  $\alpha_{\text{CO}}$ , which would bring the simulation predicted relation rightward to become more aligned with our observed  $\alpha_{\text{CO}}$ . On the other hand, the simulation from Narayanan et al. (2012) gives larger  $\alpha_{\text{CO}}$  than our modeled results. We note that  $\alpha_{\text{CO}}$  at kpc scale in Narayanan et al. (2012) is calculated as the CO  $J=1-0$  intensity averaged value of  $\alpha_{\text{CO}}$  of individual clouds, which is similar to what we did to calculate  $\langle\alpha_{\text{CO},150\text{pc}}\rangle_{1\text{kpc}}$  in Section 6.2. Therefore, the discrepancy might be due to our inclusion of diffuse molecular gas component that brings down the  $\alpha_{\text{CO}}$  values. It is also possible that the true  $x_{\text{CO}}$  is slightly lower than  $3 \times 10^{-4}$  and the actual  $\alpha_{\text{CO}}$  in the Antennae might be higher than our derived values.

In the right panel of Fig. 18, we show  $\alpha_{\text{CO}}$  versus the total surface density and compare it with the empirical relation by Bolatto et al. (2013). The absolute  $\alpha_{\text{CO}}$  values are generally consistent with the theoretical expectation but with a large scatter. We also do not see a significant correlation between these two quantities for the Antennae alone (Pearson coefficient of -0.11)

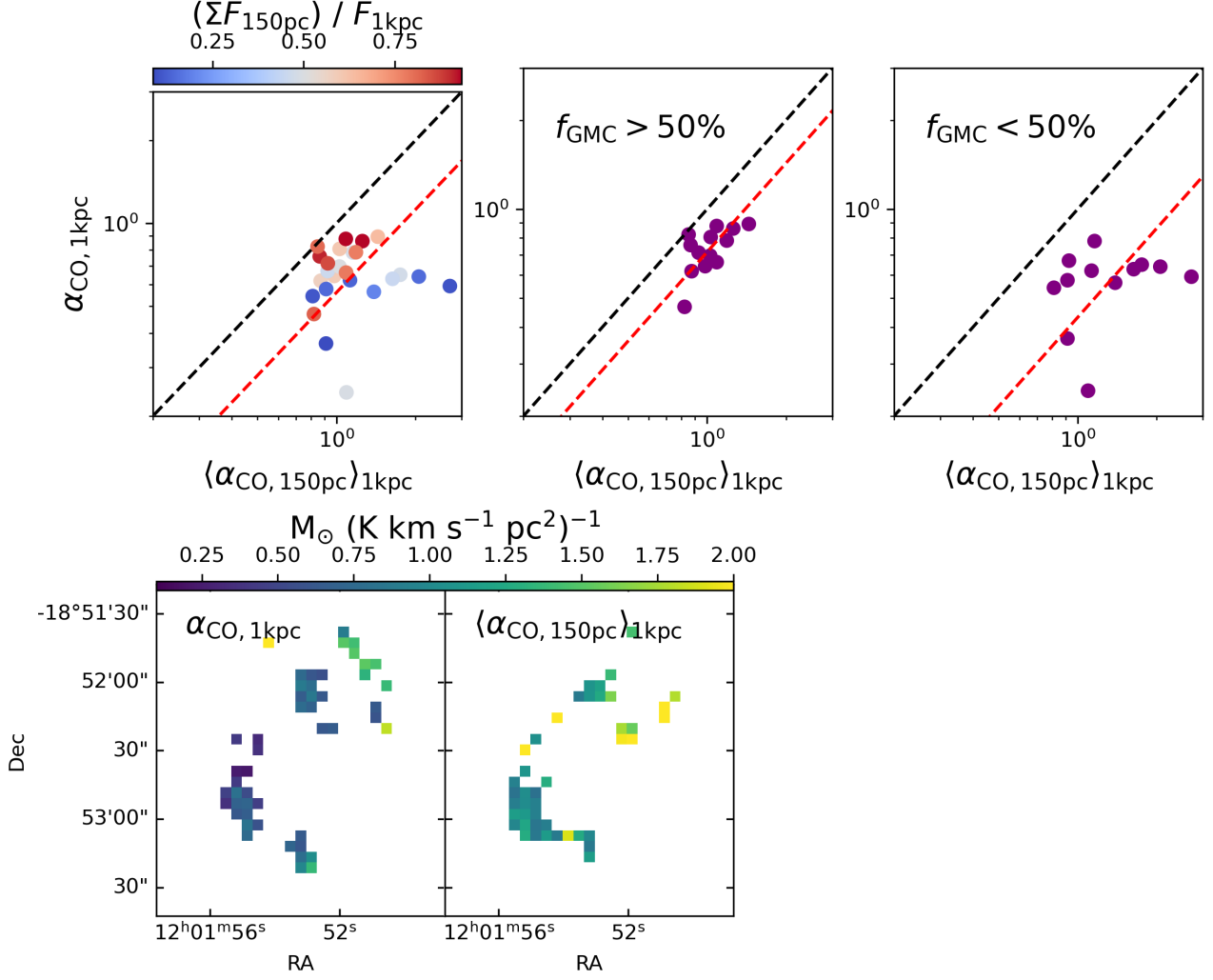


**Figure 17.** ((Top) The comparison between  $\alpha_{\text{CO}}$  at kpc scale ( $\alpha_{\text{CO}, 1\text{kpc}}$ ) and  $\alpha_{\text{CO}}$  at 150 pc scale intensity averaged over kpc scale pixels ( $\langle \alpha_{\text{CO}, 150\text{pc}} \rangle_{1\text{kpc}}$ ). Pixels are color coded by the fraction of CO  $J=1-0$  emission at kpc scale that comes from GMC scales for each pixel ( $f_{\text{GMC}}$ , see text for detailed description). The black dashed line is the one-to-one while the red dashed line is the proportional fit to the data. The middle and right panels show the data points with  $f_{\text{GMC}}$  greater and smaller than 50%, respectively. We can see that the higher fraction of the GMC-scale emission at kpc scale roughly corresponds to higher  $\alpha_{\text{CO}, 1\text{kpc}} / \langle \alpha_{\text{CO}, 150\text{pc}} \rangle_{1\text{kpc}}$  ratio, which suggests diffuse gas component might play a role in bringing down the  $\alpha_{\text{CO}, 1\text{kpc}}$ . (Bottom) Maps of  $\alpha_{\text{CO}, 1\text{kpc}}$  and  $\langle \alpha_{\text{CO}, 150\text{pc}} \rangle_{1\text{kpc}}$ .

or the Antennae and other U/LIRGs combined (Pearson coefficient of -0.16). Therefore, it is possible that  $\alpha_{\text{CO}}$  just has a bimodal distribution among normal spirals and U/LIRGs instead of a continuous dependence on the total surface densities. We also note that the  $\alpha_{\text{CO}}$  derived in Sandstrom et al. (2013a) uses the gas-to-dust ratio while the  $\alpha_{\text{CO}}$  derived in the Antennae and U/LIRGs are based on LVG modeling; these different approaches may introduce some systematic uncertainties in  $\alpha_{\text{CO}}$  comparison.

## 7. CONCLUSIONS

In this paper, we have constrained the spatial variation of the CO-to- $\text{H}_2$  conversion,  $\alpha_{\text{CO}}$ , in the Antennae merger at both GMC and kpc scales based on high-resolution ALMA CO and  $^{13}\text{CO}$  lines. Our main conclusions are summarized below.

- The CO  $J=2-1/1-0$  ( $\sim 1$ ) and CO  $J=3-2/1-0$  ( $\sim 0.7$ ) ratios in the Antennae are significantly higher than the commonly observed ratio in normal spiral galaxies (Leroy et al. 2021; Wilson et al. 2012; Leroy et al. 2022). These large ratios suggest that molecular gas in this starburst system has higher volume density and/or kinetic temperature compared to normal spiral galaxies. In contrast, the

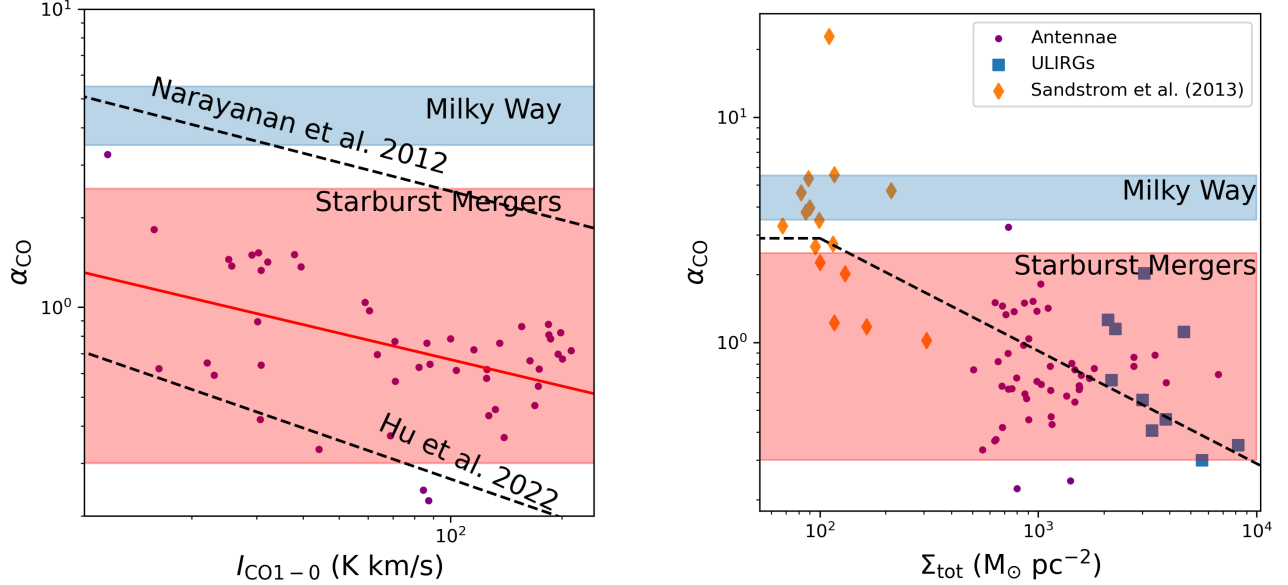


**Figure 18.** (Left) Modeled  $\alpha_{\text{CO}}$  versus CO  $J=1-0$  integrated intensity  $I_{\text{CO}(1-0)}$  at 1 kpc resolution. The red solid line is the power law fit to the data while the dashed lines are the simulation predicted relations from Narayanan et al. (2012) and Hu et al. (2022), respectively. We can see our fit relation has similar slope as the simulation predictions. (Right) Modeled  $\alpha_{\text{CO}}$  versus total surface density for the Antennae (purple), normal spiral galaxies (orange diamonds) and ULIRGs (blue squares). The dashed line is the prescription from Bolatto et al. (2013). We can see that the absolute value of  $\alpha_{\text{CO}}$  in the Antennae is generally consistent with the prediction of this prescription. However, we do not see a significant correlation between  $\alpha_{\text{CO}}$  and the total surface density for the Antennae alone.

- $^{13}\text{CO}/\text{CO } J=1-0$  and  $^{13}\text{CO}/\text{CO } J=2-1$  ratios ( $\sim 0.1$ ) in the Antennae are similar to those in normal spiral galaxies (Cormier et al. 2018). However, the two ratio values are probably resulted from compensation effect from larger CO optical depth and  $X_{12/13}$  of the Antennae than those of normal spiral galaxies. We also suspect that the  $^{13}\text{CO}/\text{CO}$  ratio in the Antennae is larger than that in U/LIRGs due larger optical depth of the Antennae that has not yet been reduced by the stellar feedback.
- We derived the first resolved  $\alpha_{\text{CO}}$  map for the Antennae down to GMC scale ( $\sim 150$  pc). We find that  $\alpha_{\text{CO}}$  has a significant anti-correlation with GMC integrated intensity,  $I_{\text{CO}(1-0)}$ , which is consistent with simulation predictions (Gong et al. 2020; Hu et al. 2022). This supports the argument that  $\alpha_{\text{CO}}$  has a continuous dependence on  $I_{\text{CO}(1-0)}$  instead of a bimodal distribution among normal spiral and starburst galaxies.
- We find that  $\alpha_{\text{CO}}$  has a strong tight linear correlation with the CO optical depth, which suggests that  $\alpha_{\text{CO}}$  variations in starburst systems are mainly driven by optical depth variations rather than kinetic temperature variation, which is consistent with  $\alpha_{\text{CO}}$  studies in normal galaxy centers (Teng et al. 2022; Teng et al. 2023). We also find

a relatively tight correlation between  $\alpha_{\text{CO}}$  and the  $^{13}\text{CO}/\text{CO } J=1-0$  ratio. This correlation is consistent with our expectation that the  $^{13}\text{CO}/\text{CO } J=1-0$  ratio can be a probe to the molecular gas optical depth. The scatter in the  $\alpha_{\text{CO}}$  versus  $^{13}\text{CO}/\text{CO } J=1-0$  ratio is mainly driven by the varying  $[\text{CO}]/[^{13}\text{CO}]$  abundance ratio.

- We find that  $\alpha_{\text{CO}}$  is also tightly related to the GMC dynamical state and shows strong anti-correlations with GMC velocity dispersion. In particular, the strong anti-correlation between  $\alpha_{\text{CO}}$  and  $\sigma_v$  has a slope consistent with theoretical prediction of -0.5. This result is consistent with previous LVG studies on U/LIRGs (e.g. Papadopoulos et al. 2012), which suggested that the low  $\alpha_{\text{CO}}$  in these systems are mainly caused by GMCs with large velocity dispersion and hence being out of virial equilibrium.
- We compare our modeled gas surface density with 345 GHz dust continuum. Our comparison shows that our chosen CO-to-H<sub>2</sub> abundance ratio  $x_{\text{CO}} = 3 \times 10^{-4}$  gives us reasonable gas-to-dust ratios of  $\sim 100$ . Given this abundance ratio choice, we would expect most  $\alpha_{\text{CO}}$  values in the Antennae are close to the typical U/LIRG value of  $1.1 M_{\odot} (\text{K km s}^{-1} \text{pc}^2)^{-1}$ . This  $\alpha_{\text{CO}}$  will put most



GMCs in the Antennae out of virial equilibrium, which is consistent with simulation prediction of GMCs in starburst mergers (He et al. 2023).

- We compare luminosity weighted GMC-scale  $\alpha_{\text{CO}}$  averaged at kpc resolution with the  $\alpha_{\text{CO}}$  that are directly derived from kpc-resolution data. Our comparison shows that kpc-scale  $\alpha_{\text{CO}}$  from LVG modeling is about 60% of the averaged values of  $\alpha_{\text{CO}}$  values of  $\alpha_{\text{CO}}$  at kpc scales. We think that the lower  $\alpha_{\text{CO}}$  at kpc scale might be due to the diffuse warm component that have intrinsically lower  $\alpha_{\text{CO}}$ .
- We also explore the dependence of modeled  $\alpha_{\text{CO}}$  at kpc scales on various observables. We find that the kpc-scale  $\alpha_{\text{CO}}$  shows a similar anti-correlation with CO intensity as predicted by simulations (e.g. Narayanan et al. 2012; Hu et al. 2022). We also tested the anti-correlation between  $\alpha_{\text{CO}}$  and total surface density,  $\Sigma_{\text{tot}}$ , as suggested in Bolatto et al. (2013). We find  $\alpha_{\text{CO}}$  of the Antennae lies along the trend with normal spiral galaxies and U/LIRGs. However, we do not see a significant correlation between  $\alpha_{\text{CO}}$  and  $\Sigma_{\text{tot}}$ , especially for the Antennae

alone or the Antennae and other U/LIRGs combined.

This paper makes the uses of the following ALMA data:

ADS/JAO.ALMA # 2018.1.00272.S

ADS/JAO.ALMA # 2021.1.00439.S. ALMA is a partnership of ESO (representing its member states), NSF (USA), and NINS (Japan), together with NRC (Canada), MOST and ASIAA (Taiwan), and KASI (Republic of Korea), in cooperation with the Republic of Chile. The Joint ALMA Observatory is operated by ESO, AUI/NRAO, and NAOJ. The National Radio Astronomy Observatory is a facility of the National Science Foundation operated under cooperative agreement by Associated Universities, Inc. This work is based in part on observations made with the Spitzer Space Telescope, which was operated by the Jet Propulsion Laboratory, California Institute of Technology under a contract with NASA.

*Facilities:* ALMA, Spitzer

*Software:* astropy (Collaboration et al. 2013)

## REFERENCES

- Abdo, A. A., Ackermann, M., Ajello, M., et al. 2010, *The Astrophysical Journal*, 710, 133, doi: [10.1088/0004-637X/710/1/133](https://doi.org/10.1088/0004-637X/710/1/133)
- Accurso, G., Saintonge, A., Catinella, B., et al. 2017, *Monthly Notices of the Royal Astronomical Society*, 470, 4750, doi: [10.1093/mnras/stx1556](https://doi.org/10.1093/mnras/stx1556)
- Amorín, R., Muñoz-Tuñón, C., Aguerri, J. A. L., & Planesas, P. 2016, *Astronomy and Astrophysics*, 588, A23, doi: [10.1051/0004-6361/201526397](https://doi.org/10.1051/0004-6361/201526397)
- Bemis, A., & Wilson, C. D. 2019, *The Astronomical Journal*, 157, 131, doi: [10.3847/1538-3881/ab041d](https://doi.org/10.3847/1538-3881/ab041d)
- Bigiel, F., Leroy, A. K., Blitz, L., et al. 2015, *The Astrophysical Journal*, 815, 103, doi: [10.1088/0004-637X/815/2/103](https://doi.org/10.1088/0004-637X/815/2/103)
- Bolatto, A. D., Leroy, A., Israel, F. P., & Jackson, J. M. 2003, *The Astrophysical Journal*, 595, 167, doi: [10.1086/377230](https://doi.org/10.1086/377230)
- Bolatto, A. D., Leroy, A. K., Rosolowsky, E., Walter, F., & Blitz, L. 2008, *The Astrophysical Journal*, 686, 948, doi: [10.1086/591513](https://doi.org/10.1086/591513)
- Bolatto, A. D., Wolfire, M., & Leroy, A. K. 2013, *Annual Review of Astronomy and Astrophysics*, 51, 207, doi: [10.1146/annurev-astro-082812-140944](https://doi.org/10.1146/annurev-astro-082812-140944)
- Boulanger, F., Abergel, A., Bernard, J. P., et al. 1996, *Astronomy and Astrophysics*, 312, 256
- Bournaud, F., Daddi, E., Weiß, A., et al. 2015, *A&A*, 575, A56, doi: [10.1051/0004-6361/201425078](https://doi.org/10.1051/0004-6361/201425078)
- Brown, T., & Wilson, C. D. 2019, *The Astrophysical Journal*, 879, 17, doi: [10.3847/1538-4357/ab2246](https://doi.org/10.3847/1538-4357/ab2246)
- Brunetti, N. 2022, Thesis
- Brunetti, N., & Wilson, C. D. 2022, *Monthly Notices of the Royal Astronomical Society*, 515, 2928, doi: [10.1093/mnras/stac1975](https://doi.org/10.1093/mnras/stac1975)
- Brunetti, N., Wilson, C. D., Sliwa, K., et al. 2020, *Monthly Notices of the Royal Astronomical Society*, 500, 4730, doi: [10.1093/mnras/staa3425](https://doi.org/10.1093/mnras/staa3425)
- Bryant, P. M., & Scoville, N. Z. 1996, *The Astrophysical Journal*, 457, 678, doi: [10.1086/176763](https://doi.org/10.1086/176763)
- . 1999, *The Astronomical Journal*, 117, 2632, doi: [10.1086/300879](https://doi.org/10.1086/300879)
- Carleton, T., Cooper, M. C., Bolatto, A. D., et al. 2017, *Monthly Notices of the Royal Astronomical Society*, 467, 4886, doi: [10.1093/mnras/stx390](https://doi.org/10.1093/mnras/stx390)
- Chandar, R., Fall, S. M., Whitmore, B. C., & Mulia, A. J. 2017, *The Astrophysical Journal*, 849, 128, doi: [10.3847/1538-4357/aa92ce](https://doi.org/10.3847/1538-4357/aa92ce)

- Collaboration, T. A., Robitaille, T. P., Tollerud, E. J., et al. 2013, *A&A*, 558, A33, doi: [10.1051/0004-6361/201322068](https://doi.org/10.1051/0004-6361/201322068)
- Cormier, D., Bigiel, F., Jiménez-Donaire, M. J., et al. 2018, *Monthly Notices of the Royal Astronomical Society*, 475, 3909, doi: [10.1093/mnras/sty059](https://doi.org/10.1093/mnras/sty059)
- Dame, T. M., Hartmann, D., & Thaddeus, P. 2001, *The Astrophysical Journal*, 547, 792, doi: [10.1086/318388](https://doi.org/10.1086/318388)
- Donovan Meyer, J., Koda, J., Momose, R., et al. 2012, *The Astrophysical Journal*, 744, 42, doi: [10.1088/0004-637X/744/1/42](https://doi.org/10.1088/0004-637X/744/1/42)
- Downes, D., & Solomon, P. M. 1998, *ApJ*, 507, 615, doi: [10.1086/306339](https://doi.org/10.1086/306339)
- Downes, D., Solomon, P. M., & Radford, S. J. E. 1993, *The Astrophysical Journal*, 414, L13, doi: [10.1086/186984](https://doi.org/10.1086/186984)
- Dunne, L., Maddox, S. J., Papadopoulos, P. P., Ivison, R. J., & Gomez, H. L. 2022, *Monthly Notices of the Royal Astronomical Society*, 517, 962, doi: [10.1093/mnras/stac2098](https://doi.org/10.1093/mnras/stac2098)
- Eskew, M., Zaritsky, D., & Meidt, S. 2012, *Astronomical Journal*, 143, 4, doi: [10.1088/0004-6256/143/6/139](https://doi.org/10.1088/0004-6256/143/6/139)
- Goldsmith, P. F., Heyer, M., Narayanan, G., et al. 2008, *The Astrophysical Journal*, 680, 428, doi: [10.1086/587166](https://doi.org/10.1086/587166)
- Gong, M., Ostriker, E. C., Kim, C.-G., & Kim, J.-G. 2020, *The Astrophysical Journal*, 903, 142, doi: [10.3847/1538-4357/abbda8](https://doi.org/10.3847/1538-4357/abbda8)
- Grenier, I. A., Casandjian, J.-M., & Terrier, R. 2005, *Science*, 307, 1292, doi: [10.1126/science.1106924](https://doi.org/10.1126/science.1106924)
- Gunawardhana, M. L. P., Brinchmann, J., Weilbacher, P. M., et al. 2020, *Monthly Notices of the Royal Astronomical Society*, 497, 3860, doi: [10.1093/mnras/staa2158](https://doi.org/10.1093/mnras/staa2158)
- Harrington, K. C., Weiss, A., Yun, M. S., et al. 2021, *The Astrophysical Journal*, 908, 95, doi: [10.3847/1538-4357/abcc01](https://doi.org/10.3847/1538-4357/abcc01)
- He, H., Bottrell, C., Wilson, C., et al. 2023, *Molecular Gas and Star Formation in Nearby Starburst Galaxy Mergers*, doi: [10.48550/arXiv.2301.13250](https://doi.org/10.48550/arXiv.2301.13250)
- He, H., Wilson, C., Brunetti, N., et al. 2022, *The Astrophysical Journal*, 928, 57, doi: [10.3847/1538-4357/ac5628](https://doi.org/10.3847/1538-4357/ac5628)
- He, H., Wilson, C. D., Sliwa, K., Iono, D., & Saito, T. 2020, *Monthly Notices of the Royal Astronomical Society*, 496, 5243, doi: [10.1093/mnras/staa1826](https://doi.org/10.1093/mnras/staa1826)
- Heyer, M. H., Carpenter, J. M., & Snell, R. L. 2001, *The Astrophysical Journal*, 551, 852, doi: [10.1086/320218](https://doi.org/10.1086/320218)
- Hu, C.-Y., Schrupa, A., Sternberg, A., & van Dishoeck, E. F. 2022, *ApJ*, 931, 28, doi: [10.3847/1538-4357/ac65fd](https://doi.org/10.3847/1538-4357/ac65fd)
- Jiménez-Donaire, M. J., Bigiel, F., Leroy, A. K., et al. 2017, *Monthly Notices of the Royal Astronomical Society*, 466, 49, doi: [10.1093/mnras/stw2996](https://doi.org/10.1093/mnras/stw2996)
- Kamenetzky, J., Rangwala, N., & Glenn, J. 2017, *Monthly Notices of the Royal Astronomical Society*, 471, 2917, doi: [10.1093/mnras/stx1595](https://doi.org/10.1093/mnras/stx1595)
- Karl, S. J., Naab, T., Johansson, P. H., et al. 2010, *The Astrophysical Journal*, 715, L88, doi: [10.1088/2041-8205/715/2/L88](https://doi.org/10.1088/2041-8205/715/2/L88)
- Kazandjian, M. V., Meijerink, R., Pelupessy, I., Israel, F. P., & Spaans, M. 2015, *Astronomy and Astrophysics*, 574, A127, doi: [10.1051/0004-6361/201322805](https://doi.org/10.1051/0004-6361/201322805)
- Keller, B. W., Wadsley, J., Benincasa, S. M., & Couchman, H. M. P. 2014, *Monthly Notices of the Royal Astronomical Society*, 442, 3013, doi: [10.1093/mnras/stu1058](https://doi.org/10.1093/mnras/stu1058)
- Klaas, U., Nielbock, M., Haas, M., Krause, O., & Schreiber, J. 2010, *Astronomy and Astrophysics*, 518, L44, doi: [10.1051/0004-6361/201014670](https://doi.org/10.1051/0004-6361/201014670)
- Langer, W. D., & Penzias, A. A. 1990, *The Astrophysical Journal*, 357, 477, doi: [10.1086/168935](https://doi.org/10.1086/168935)
- Leroy, A. K., Bolatto, A., Gordon, K., et al. 2011, *The Astrophysical Journal*, 737, 12, doi: [10.1088/0004-637X/737/1/12](https://doi.org/10.1088/0004-637X/737/1/12)
- Leroy, A. K., Usero, A., Schrupa, A., et al. 2017, *The Astrophysical Journal*, 835, 217, doi: [10.3847/1538-4357/835/2/217](https://doi.org/10.3847/1538-4357/835/2/217)
- Leroy, A. K., Schinnerer, E., Hughes, A., et al. 2021, *ApJS*, 257, 43, doi: [10.3847/1538-4365/ac17f3](https://doi.org/10.3847/1538-4365/ac17f3)
- Leroy, A. K., Rosolowsky, E., Usero, A., et al. 2022, *The Astrophysical Journal*, 927, 149, doi: [10.3847/1538-4357/ac3490](https://doi.org/10.3847/1538-4357/ac3490)
- Li, Z., Li, Z., Smith, M. W. L., et al. 2020, *Monthly Notices of the Royal Astronomical Society*, 492, 195, doi: [10.1093/mnras/stz3409](https://doi.org/10.1093/mnras/stz3409)
- Magnelli, B., Saintonge, A., Lutz, D., et al. 2012, *Astronomy and Astrophysics*, 548, A22, doi: [10.1051/0004-6361/201220074](https://doi.org/10.1051/0004-6361/201220074)
- Maloney, P. 1990, *The Astrophysical Journal*, 348, L9, doi: [10.1086/185618](https://doi.org/10.1086/185618)
- Matsushita, S., Iono, D., Petitpas, G. R., et al. 2009, *Astrophysical Journal*, 693, 56, doi: [10.1088/0004-637X/693/1/56](https://doi.org/10.1088/0004-637X/693/1/56)
- Milam, S. N., Savage, C., Brewster, M. A., Ziurys, L. M., & Wyckoff, S. 2005, *The Astrophysical Journal*, 634, 1126, doi: [10.1086/497123](https://doi.org/10.1086/497123)
- Mok, A., Chandar, R., & Fall, S. M. 2020, *The Astrophysical Journal*, 893, 135, doi: [10.3847/1538-4357/ab7a14](https://doi.org/10.3847/1538-4357/ab7a14)
- Montoya Arroyave, I., Ciccone, C., Makroleivaditi, E., et al. 2023, *Astronomy and Astrophysics*, 673, A13, doi: [10.1051/0004-6361/202245046](https://doi.org/10.1051/0004-6361/202245046)

- Narayanan, D., Krumholz, M., Ostriker, E. C., & Hernquist, L. 2011, *Monthly Notices of the Royal Astronomical Society*, 418, 664, doi: [10.1111/j.1365-2966.2011.19516.x](https://doi.org/10.1111/j.1365-2966.2011.19516.x)
- Narayanan, D., Krumholz, M. R., Ostriker, E. C., & Hernquist, L. 2012, *Monthly Notices of the Royal Astronomical Society*, 421, 3127, doi: [10.1111/j.1365-2966.2012.20536.x](https://doi.org/10.1111/j.1365-2966.2012.20536.x)
- Olsen, K. P., Greve, T. R., Brinch, C., et al. 2016, *Monthly Notices of the Royal Astronomical Society*, 457, 3306, doi: [10.1093/mnras/stw162](https://doi.org/10.1093/mnras/stw162)
- Papadopoulos, P. P., van der Werf, P. P., Xilouris, E. M., et al. 2012, *Monthly Notices of the Royal Astronomical Society*, 426, 2601, doi: [10.1111/j.1365-2966.2012.21001.x](https://doi.org/10.1111/j.1365-2966.2012.21001.x)
- Pessa, I., Schinnerer, E., Belfiore, F., et al. 2021, *Astronomy and Astrophysics*, 650, A134, doi: [10.1051/0004-6361/202140733](https://doi.org/10.1051/0004-6361/202140733)
- Planck Collaboration, Ade, P. A. R., Aghanim, N., et al. 2011, *Astronomy and Astrophysics*, 536, A19, doi: [10.1051/0004-6361/201116479](https://doi.org/10.1051/0004-6361/201116479)
- Privon, G. C., Barnes, J. E., Evans, A. S., et al. 2013, *Astrophysical Journal*, 771, doi: [10.1088/0004-637X/771/2/120](https://doi.org/10.1088/0004-637X/771/2/120)
- Ramambason, L., Lebouteiller, V., Madden, S. C., et al. 2023, *Molecular Gas Distribution and CO-to-H<sub>2</sub> Conversion Factors in CO-faint Low-Metallicity Dwarf Galaxies*, doi: [10.48550/arXiv.2306.14881](https://doi.org/10.48550/arXiv.2306.14881)
- Rebolledo, D., Wong, T., Leroy, A., Koda, J., & Donovan Meyer, J. 2012, *The Astrophysical Journal*, 757, 155, doi: [10.1088/0004-637X/757/2/155](https://doi.org/10.1088/0004-637X/757/2/155)
- Remy, Q., Grenier, I. A., Marshall, D. J., & Casandjian, J. M. 2017, *Astronomy and Astrophysics*, 601, A78, doi: [10.1051/0004-6361/201629632](https://doi.org/10.1051/0004-6361/201629632)
- Renaud, F., Bournaud, F., Agertz, O., et al. 2019a, *Astronomy & Astrophysics*, 625, A65, doi: [10.1051/0004-6361/201935222](https://doi.org/10.1051/0004-6361/201935222)
- Renaud, F., Bournaud, F., Daddi, E., & Weiß, A. 2019b, *Astronomy & Astrophysics*, Volume 621, id.A104, <NUPAGES>5</NUPAGES> pp., 621, A104, doi: [10.1051/0004-6361/201834397](https://doi.org/10.1051/0004-6361/201834397)
- Salak, D., Nakai, N., Seta, M., & Miyamoto, Y. 2019, *The Astrophysical Journal*, 887, 143, doi: [10.3847/1538-4357/ab55dc](https://doi.org/10.3847/1538-4357/ab55dc)
- Sandstrom, K. M., Leroy, A. K., Walter, F., et al. 2013a, *The Astrophysical Journal*, 777, 5, doi: [10.1088/0004-637X/777/1/5](https://doi.org/10.1088/0004-637X/777/1/5)
- . 2013b, *The Astrophysical Journal*, 777, 5, doi: [10.1088/0004-637X/777/1/5](https://doi.org/10.1088/0004-637X/777/1/5)
- Sargent, M. T., Daddi, E., Béthermin, M., et al. 2014, *Astrophysical Journal*, 793, doi: [10.1088/0004-637X/793/1/19](https://doi.org/10.1088/0004-637X/793/1/19)
- Schirm, M. R. P., Wilson, C. D., Parkin, T. J., et al. 2014, *The Astrophysical Journal*, 781, 101, doi: [10.1088/0004-637X/781/2/101](https://doi.org/10.1088/0004-637X/781/2/101)
- Schruba, A., Leroy, A. K., Walter, F., et al. 2012, *The Astrophysical Journal*, 143, 138, doi: [10.1088/0004-6256/143/6/138](https://doi.org/10.1088/0004-6256/143/6/138)
- Schweizer, F., Burns, C. R., Madore, B. F., et al. 2008, *The Astrophysical Journal*, 136, 1482, doi: [10.1088/0004-6256/136/4/1482](https://doi.org/10.1088/0004-6256/136/4/1482)
- Scoville, N. Z., & Good, J. C. 1989, *The Astrophysical Journal*, 339, 149, doi: [10.1086/167283](https://doi.org/10.1086/167283)
- Scoville, N. Z., Yun, M. S., Clemens, D. P., Sanders, D. B., & Waller, W. H. 1987, *The Astrophysical Journal Supplement Series*, 63, 821, doi: [10.1086/191185](https://doi.org/10.1086/191185)
- Shetty, R., Glover, S. C., Dullemond, C. P., et al. 2011, *Monthly Notices of the Royal Astronomical Society*, 415, 3253, doi: [10.1111/j.1365-2966.2011.18937.x](https://doi.org/10.1111/j.1365-2966.2011.18937.x)
- Sliwa, K., & Downes, D. 2017, *Astronomy & Astrophysics*, Volume 604, id.A2, <NUPAGES>16</NUPAGES> pp., 604, A2, doi: [10.1051/0004-6361/201630139](https://doi.org/10.1051/0004-6361/201630139)
- Sliwa, K., Wilson, C. D., Aalto, S., & Privon, G. C. 2017a, *The Astrophysical Journal*, 840, L11, doi: [10.3847/2041-8213/aa6ea4](https://doi.org/10.3847/2041-8213/aa6ea4)
- Sliwa, K., Wilson, C. D., Iono, D., Peck, A., & Matsushita, S. 2014, *The Astrophysical Journal*, 796, L15, doi: [10.1088/2041-8205/796/1/L15](https://doi.org/10.1088/2041-8205/796/1/L15)
- Sliwa, K., Wilson, C. D., Matsushita, S., et al. 2017b, *The Astrophysical Journal*, 840, 8, doi: [10.3847/1538-4357/aa689b](https://doi.org/10.3847/1538-4357/aa689b)
- Sliwa, K., Wilson, C. D., Petitpas, G. R., et al. 2012, *Astrophysical Journal*, 753, doi: [10.1088/0004-637X/753/1/46](https://doi.org/10.1088/0004-637X/753/1/46)
- Sliwa, K., Wilson, C. D., Krips, M., et al. 2013, *Astrophysical Journal*, 777, doi: [10.1088/0004-637X/777/2/126](https://doi.org/10.1088/0004-637X/777/2/126)
- Sofia, U. J., Lauroesch, J. T., Meyer, D. M., & Cartledge, S. I. B. 2004, *The Astrophysical Journal*, 605, 272, doi: [10.1086/382592](https://doi.org/10.1086/382592)
- Solomon, P. M., Downes, D., Radford, S. J. E., & Barrett, J. W. 1997, *The Astrophysical Journal*, 478, 144, doi: [10.1086/303765](https://doi.org/10.1086/303765)
- Solomon, P. M., Rivolo, A. R., Barrett, J., & Yahil, A. 1987, *The Astrophysical Journal*, 319, 730, doi: [10.1086/165493](https://doi.org/10.1086/165493)
- Solomon, P. M., & Vanden Bout, P. A. 2005, *Annual Review of Astronomy and Astrophysics*, 43, 677, doi: [10.1146/annurev.astro.43.051804.102221](https://doi.org/10.1146/annurev.astro.43.051804.102221)
- Strong, A. W., & Mattox, J. R. 1996, *Astronomy and Astrophysics*, 308, L21

- Sun, J., Leroy, A. K., Schrubba, A., et al. 2018, *The Astrophysical Journal*, 860, 172, doi: [10.3847/1538-4357/aac326](https://doi.org/10.3847/1538-4357/aac326)
- Sun, J., Leroy, A. K., Schinnerer, E., et al. 2020a, *ApJL*, 901, L8, doi: [10.3847/2041-8213/abb3be](https://doi.org/10.3847/2041-8213/abb3be)
- Sun, J., Leroy, A. K., Ostriker, E. C., et al. 2020b, *ApJ*, 892, 148, doi: [10.3847/1538-4357/ab781c](https://doi.org/10.3847/1538-4357/ab781c)
- Sun, J., Leroy, A. K., Rosolowsky, E., et al. 2022, *The Astronomical Journal*, 164, 43, doi: [10.3847/1538-3881/ac74bd](https://doi.org/10.3847/1538-3881/ac74bd)
- Sun, J., Leroy, A. K., Ostriker, E. C., et al. 2023, *Star Formation Laws and Efficiencies across 80 Nearby Galaxies*, doi: [10.48550/arXiv.2302.12267](https://doi.org/10.48550/arXiv.2302.12267)
- Teng, Y.-H., Sandstrom, K. M., Sun, J., et al. 2022, *The Astrophysical Journal*, 925, 72, doi: [10.3847/1538-4357/ac382f](https://doi.org/10.3847/1538-4357/ac382f)
- Teng, Y.-H., Sandstrom, K. M., Sun, J., et al. 2023, *ApJ*, 950, 119, doi: [10.3847/1538-4357/accb86](https://doi.org/10.3847/1538-4357/accb86)
- Teng, Y.-H., Chiang, I. D., Sandstrom, K. M., et al. 2024, *The Astrophysical Journal*, 961, 42, doi: [10.3847/1538-4357/ad10ae](https://doi.org/10.3847/1538-4357/ad10ae)
- Ueda, J., Iono, D., Petitpas, G., et al. 2012, *The Astrophysical Journal*, 745, 65, doi: [10.1088/0004-637X/745/1/65](https://doi.org/10.1088/0004-637X/745/1/65)
- Van Der Tak, F. F., Black, J. H., Schöier, F. L., Jansen, D. J., & Van Dishoeck, E. F. 2007, *Astronomy and Astrophysics*, 468, 627, doi: [10.1051/0004-6361:20066820](https://doi.org/10.1051/0004-6361:20066820)
- Vigroux, L., Audouze, J., & Lequeux, J. 1976, *Astronomy and Astrophysics*, 52, 1
- Vlahakis, C., van der Werf, P., Israel, F. P., & Tilanus, R. P. J. 2013, *Monthly Notices of the Royal Astronomical Society*, 433, 1837, doi: [10.1093/mnras/stt841](https://doi.org/10.1093/mnras/stt841)
- Whitmore, B. C., Brogan, C., Chandar, R., et al. 2014, *ApJ*, 795, 156, doi: [10.1088/0004-637X/795/2/156](https://doi.org/10.1088/0004-637X/795/2/156)
- Wilson, C. D., Rangwala, N., Glenn, J., et al. 2014, *The Astrophysical Journal*, 789, L36, doi: [10.1088/2041-8205/789/2/L36](https://doi.org/10.1088/2041-8205/789/2/L36)
- Wilson, C. D., Scoville, N., Madden, S. C., & Charmandaris, V. 2003, *The Astrophysical Journal*, 599, 1049, doi: [10.1086/379344](https://doi.org/10.1086/379344)
- Wilson, C. D., Petitpas, G. R., Iono, D., et al. 2008, *The Astrophysical Journal Supplement Series*, 178, 189, doi: [10.1086/590910](https://doi.org/10.1086/590910)
- Wilson, C. D., Warren, B. E., Israel, F. P., et al. 2012, *Monthly Notices of the Royal Astronomical Society*, 424, 3050, doi: [10.1111/j.1365-2966.2012.21453.x](https://doi.org/10.1111/j.1365-2966.2012.21453.x)
- Wolfire, M. G., Hollenbach, D., & McKee, C. F. 2010, *The Astrophysical Journal*, 716, 1191, doi: [10.1088/0004-637X/716/2/1191](https://doi.org/10.1088/0004-637X/716/2/1191)
- Young, J. S., & Scoville, N. Z. 1991, *Annual Review of Astronomy and Astrophysics*, 29, 581, doi: [10.1146/annurev.aa.29.090191.003053](https://doi.org/10.1146/annurev.aa.29.090191.003053)
- Zhang, Q., Fall, S. M., & Whitmore, B. C. 2001, *Observatory*, 10
- Zhu, M., Seaquist, E. R., & Kuno, N. 2003, *The Astrophysical Journal*, 588, 243, doi: [10.1086/368353](https://doi.org/10.1086/368353)

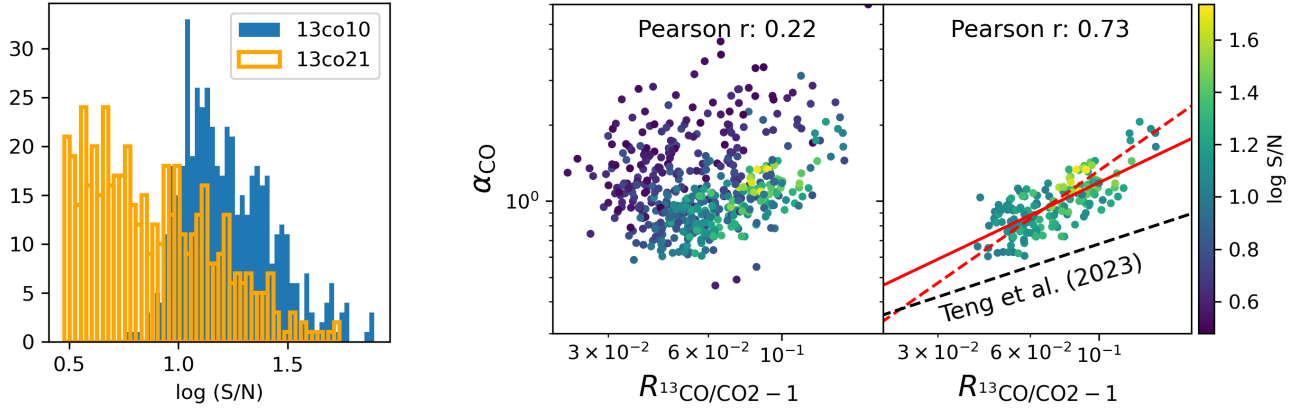


**Figure A1.** (Left) The logarithm of S/N distribution of  $^{13}\text{CO}$   $J=1-0$  and  $J=2-1$  for pixels with good  $\alpha_{\text{CO}}$  constraint. We can see most pixels have  $^{13}\text{CO}$   $J=1-0$  S/N level greater than 10. In contrast, majority of pixels have  $^{13}\text{CO}$   $J=2-1$  S/N level less than 10. (Right) The  $\alpha_{\text{CO}}$  versus the  $^{13}\text{CO}/\text{CO}$   $J=2-1$  ratio for all pixels with good  $\alpha_{\text{CO}}$  constraint (left panel) and for pixels with  $^{13}\text{CO}$   $J=2-1$  S/N level greater than 10 (right panel). The red solid line is the power-law fit for  $\alpha_{\text{CO}}$  versus  $R_{^{13}\text{CO}/\text{CO}2-1}$  relation while the red dashed line is the fit for  $\alpha_{\text{CO}}$  versus  $R_{^{13}\text{CO}/\text{CO}1-0}$  relation. The black dashed line is the relation from Teng et al. (2023). We can see that by removing low S/N pixels,  $\alpha_{\text{CO}}$  also has a tight correlation with  $^{13}\text{CO}/\text{CO}$  2-1 ratio.

## APPENDIX

### A. $\alpha_{\text{CO}}$ VERSUS $^{13}\text{CO}/\text{CO}$ $J=2-1$ RATIO

We find a strong correlation between  $\alpha_{\text{CO}}$  and  $^{13}\text{CO}/\text{CO}$   $J=1-0$  ratio, which is consistent with the literature findings (Teng et al. 2022; Teng et al. 2023). However, we see that our  $\alpha_{\text{CO}}$  versus  $R_{^{13}\text{CO}/\text{CO}1-0}$  relation has a steeper slope and than the  $\alpha_{\text{CO}}$  versus  $R_{^{13}\text{CO}/\text{CO}2-1}$  relation found in (Teng et al. 2022; Teng et al. 2023). One possible reason for the difference might be due to our different choice of excitation lines. To test this, we also plot the  $\alpha_{\text{CO}}$  versus  $R_{^{13}\text{CO}/\text{CO}2-1}$  for the Antennae in Fig. A1. We can see that if we include all the data points from Fig. 11, we have a weak if not none correlation between  $\alpha_{\text{CO}}$  and  $R_{^{13}\text{CO}/\text{CO}2-1}$ . We note that our  $^{13}\text{CO}$   $J=2-1$  observation has a much lower sensitivity than the  $^{13}\text{CO}$   $J=1-0$  observation, which brings much larger scatter in the observed  $R_{^{13}\text{CO}/\text{CO}2-1}$ . In the left panel of Fig. A1, we show the S/N distribution for  $^{13}\text{CO}$   $J=1-0$  and  $J=2-1$  data. We can clearly see that most ( $\sim 90\%$ ) of  $^{13}\text{CO}$   $J=1-0$  data has S/N level greater than 10 while less than half ( $\sim 30\%$ ) of  $^{13}\text{CO}$   $J=2-1$  data achieve the same S/N level. In our  $\alpha_{\text{CO}}$  versus  $R_{^{13}\text{CO}/\text{CO}2-1}$  color coded by the S/N level, we see most points that cause the scatter has S/N less than 10. If we remove those pixels with S/N smaller than 10, we see a much stronger correlation between  $\alpha_{\text{CO}}$  and  $R_{^{13}\text{CO}/\text{CO}2-1}$  with a Pearson correlation coefficient of 0.7, similar to the coefficient of  $\alpha_{\text{CO}}$  versus  $R_{^{13}\text{CO}/\text{CO}1-0}$ . This suggests that we need  $^{13}\text{CO}$  data

with high sensitivity in order to use  $^{13}\text{CO}/\text{CO}$  ratio to calibrate  $\alpha_{\text{CO}}$ .

We perform the same power-law fit to the  $\alpha_{\text{CO}}$  versus  $R_{^{13}\text{CO}/\text{CO}2-1}$  for pixels with  $\text{S/N} > 10$ , as shown in the rightmost panel in Fig. A1. The function is

$$\log \alpha_{\text{CO}} = 0.58(\pm 0.04) \log R_{^{13}\text{CO}/\text{CO}2-1} + 0.65(\pm 0.05) \quad (\text{A1})$$

We also overlay the  $\alpha_{\text{CO}}$  versus  $R_{^{13}\text{CO}/\text{CO}1-0}$  relation in the same figure panel. We can see the  $^{13}\text{CO}/\text{CO}$   $J=2-1$  ratio gives a shallower slope than that of  $^{13}\text{CO}/\text{CO}$   $J=1-0$  ratio. It is possible that the shallower slope is due to a larger fraction of  $^{13}\text{CO}$   $J=2-1$  lines being subthermally excited. In the subthermal case,  $^{13}\text{CO}/\text{CO}$  ratio might also track the temperature/volume density variation as the  $T_{\text{ex}}$  for the two lines cannot be canceled out (see Eq. 12). Hence,  $^{13}\text{CO}/\text{CO}$   $J=2-1$  ratio might have a less steeper dependence on the optical depth, which is tightly correlated with  $\alpha_{\text{CO}}$ . This could result in a shallower slope for  $\alpha_{\text{CO}}$  versus  $^{13}\text{CO}/\text{CO}$   $J=2-1$  ratio.